Stem Cell Reports
Article

OPEN ACCESS

Ebola virus infection induces a delayed type I IFN response in bystander cells and the shutdown of key liver genes in human iPSC-derived hepatocytes

Whitney A. Scoon,[1,2,3] Liliana Mancio-Silva,[4] Ellen L. Suder,[2,3] Carlos Villacorta-Martin,[1] Jonathan Lindstrom-Vautrin,[1] John G. Bernbaum,[5] Steve Mazur,[5] Reed F. Johnson,[5,6] Judith Olejnik,[2,3] Elizabeth Y. Flores,[1,2,3] Aditya Mithal,[1,3] Feiya Wang,[1] Adam J. Hume,[2,3] Joseph E. Kaserman,[1,7] Sandra March-Riera,[4] Andrew A. Wilson,[1,7] Sangeeta N. Bhatia,[4,8,9,10,11] Elke Mühlberger,[2,3,*] and Gustavo Mostoslavsky[1,2,3,12,*]

[1]Center for Regenerative Medicine (CReM), Boston University and Boston Medical Center, 670 Albany Street, Suite 209, Boston, MA 02118, USA
[2]National Emerging Infectious Diseases Laboratories (NEIDL), Boston University, 620 Albany Street, Boston, MA 02118, USA
[3]Department of Microbiology, Boston University School of Medicine, 620 Albany Street, Boston, MA 02118, USA
[4]Institute for Medical Engineering and Science, Massachusetts Institute of Technology, Cambridge, MA, MA 02139, USA
[5]Integrated Research Facility, Division of Clinical Research, National Institute for Allergy and Infectious Disease, National Institutes of Health, Frederick, MD 21702, USA
[6]Emerging Viral Pathogens Section, Laboratory of Immunoregulation, Division of Intramural Research, National Institute for Allergy and Infectious Disease, National Institutes of Health, Frederick, MD 21702, USA
[7]The Pulmonary Center and Department of Medicine, Boston University School of Medicine, Boston, MA 02118, USA
[8]Koch Institute for Integrative Cancer Research, Cambridge, MA 02139, USA
[9]Broad Institute, Cambridge, MA 02139, USA
[10]Department of Medicine, Brigham and Women's Hospital, Boston, MA 02115, USA
[11]Howard Hughes Medical Institute, Chevy Chase, MD 20815, USA
[12]Section of Gastroenterology, Department of Medicine, Boston University School of Medicine, 670 Albany Street, Suite 209, Boston, MA 02118, USA
*Correspondence: muehlber@bu.edu (E.M.), gmostosl@bu.edu (G.M.)
https://doi.org/10.1016/j.stemcr.2022.08.003

SUMMARY

Liver damage and an exacerbated inflammatory response are hallmarks of Ebola virus (EBOV) infection. Little is known about the intrinsic response to infection in human hepatocytes and their contribution to inflammation. Here, we present an induced pluripotent stem cell (iPSC)-derived hepatocyte-like cell (HLC) platform to define the hepato-intrinsic response to EBOV infection. We used this platform to show robust EBOV infection, with characteristic ultrastructural changes and evidence for viral replication. Transcriptomics analysis revealed a delayed response with minimal early transcriptomic changes, followed by a general downregulation of hepatic function and upregulation of interferon signaling, providing a potential mechanism by which hepatocytes participate in disease severity and liver damage. Using RNA-fluorescence *in situ* hybridization (FISH), we showed that *IFNB1* and *CXCL10* were mainly expressed in non-infected bystander cells. We did not observe an inflammatory signature during infection. In conclusion, iPSC-HLCs are an immune competent platform to study responses to EBOV infection.

INTRODUCTION

Ebola virus (EBOV) infection causes a severe disease in humans with case fatality rates ranging from 40% to 90%. Severe liver damage, coagulopathy, and thrombocytopenia are hallmark clinical manifestations of EBOV disease (EVD) (Martines et al., 2015). Histopathological changes in liver autopsies of fatal EBOV cases include hepatocellular necrosis, Councilman bodies, Kupffer cell hyperplasia, and the presence of EBOV inclusions in infected cells (Martines et al., 2015; Zaki and Goldsmith, 1999). Liver damage in EVD patients and experimentally infected non-human primates (NHPs) is indicated by elevated serum levels of liver enzymes, including aspartate aminotransferase (AST), alanine aminotransferase (ALT), alkaline phosphatase, and γ-glutamyltransferase, and decreasing levels of albumin and calcium (de Wit et al., 2016; Geisbert et al., 2003d; Lanini et al., 2018; Rollin et al., 2007; Uyeki et al., 2016). Decreasing serum protein C levels and increasing fibrinogen levels indicate dysregulation of clotting and coagulopathy (Geisbert et al., 2003c; Liu et al., 2017; Smither et al., 2019).

In addition to organ damage, there is evidence that a dysregulated proinflammatory response is a hallmark of severe EVD (Liu et al., 2017). Monocytes and macrophages are activated upon EBOV infection (reviewed in McElroy et al., 2018), and this proinflammatory environment may affect liver damage during EBOV infection. While hepatocytes constitute over 80% of the liver volume, their immune response to EBOV has yet to be characterized. Most previous reports that have examined the intrinsic hepatic response to EBOV infection utilized immortalized hepatocarcinoma cell lines (Hartman et al., 2008; Holzer et al., 2016; Kash et al., 2006; Kuzmin et al., 2017), which have an impaired antiviral response compared with primary human hepatocytes (PHHs) (Li et al., 2005; Marozin et al., 2008). While PHHs represent a more reliable platform, limited accessibility, donor-to-donor variability, and complex *in vitro* conditions

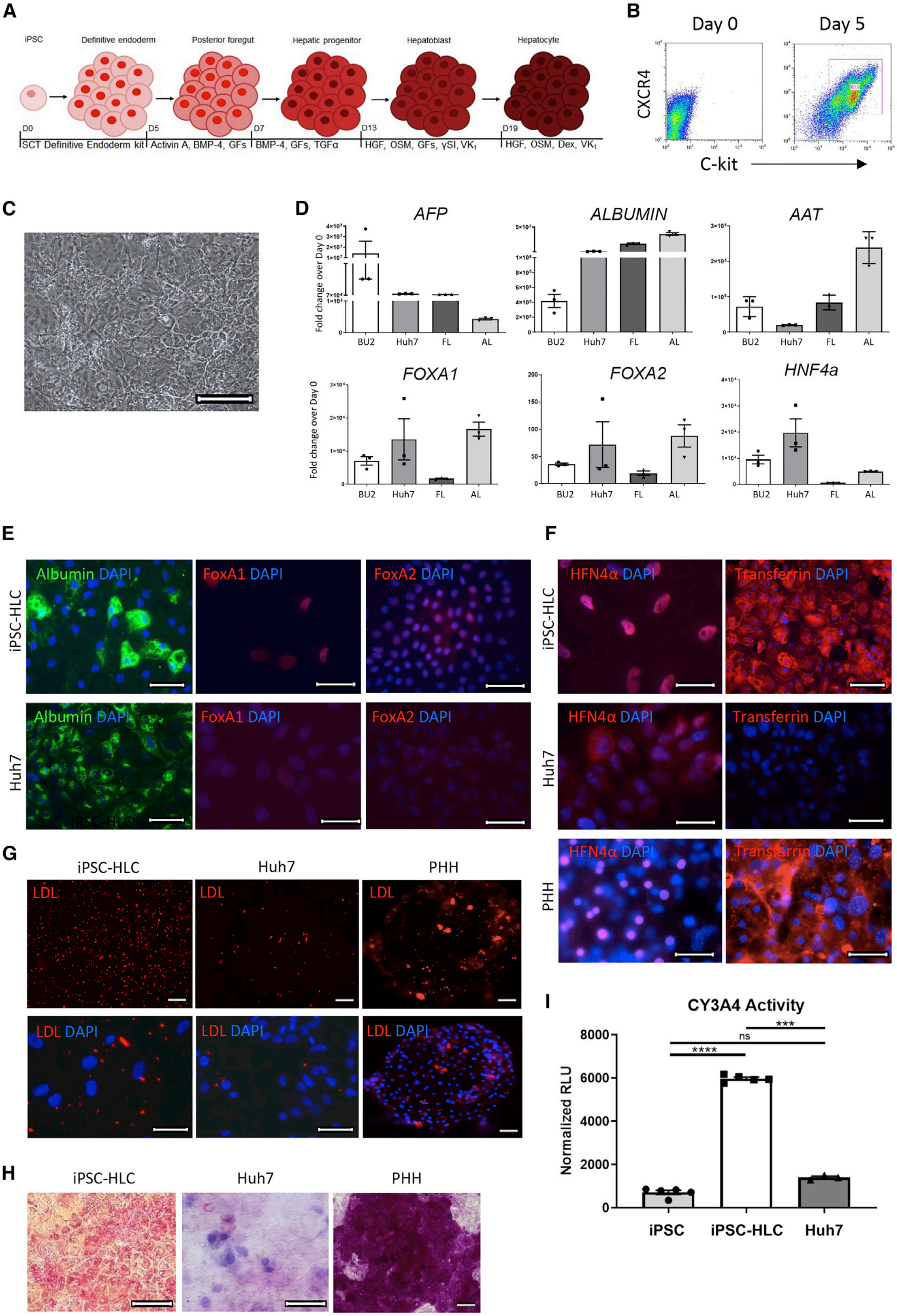

(legend on next page)

required for long-term culture have restricted their use (Gural et al., 2018; Khetani and Bhatia, 2008; March et al., 2015; Michailidis et al., 2020).

Here, we have employed human induced pluripotent stem cell (iPSC)-derived hepatocyte-like cells (HLCs) as a model for EBOV infection. These cells can be terminally differentiated and maintained in a monoculture for approximately 10 days and have previously been shown to effectively model viral infections (Lang et al., 2016; Sakurai et al., 2017; Schwartz et al., 2012; Shlomai et al., 2014; Tricot et al., 2018; Wilson et al., 2015; Zhou et al., 2014). We demonstrate that iPSC-HLCs recapitulate aspects of the innate human host response to EBOV infection that cannot be modeled in immortalized cell lines. Our data show that EBOV infection leads to a delayed type I interferon (IFN) response and the downregulation of genes associated with liver function in iPSC-HLCs, illuminating a mechanism by which hepatocytes participate in EVD severity and liver damage.

RESULTS

iPSC-derived HLCs are physiologically more similar to primary hepatocytes than immortalized Huh7 cells

To generate human HLCs from iPSCs, we used a previously published stepwise directed differentiation protocol that follows normal hepatic development as a roadmap for iPSC lineage specification (Figure 1A) (Wilson et al., 2015). At day 5 (D5), approximately 80%–90% of the cells were CXCR4/cKit double positive, indicating robust differentiation into definitive endoderm (Figure 1B). By D20 of differentiation, most cells in culture adopted a cuboidal, highly vacuolated morphology, typical of primary hepatocytes (Figure 1C). A molecular, histological, and functional characterization of the iPSC-HLCs in comparison with either immortalized hepatocarcinoma Huh7 cells or fetal and adult liver tissue showed that the iPSC-HLCs retained expression of the fetal liver marker alpha feto protein (AFP), likely reflecting the embryonic-like characteristics of the cells in this culture system (Figure 1D). As expected, iPSC-HLCs expressed many hepatic markers, including albumin, AAT, and the transcription factors FOXA1, FOXA2, and HNF4a. The mRNA levels of these hepatic markers were generally higher in Huh7 cells compared with iPSC-HLCs. However, immunofluorescence analysis revealed striking differences in the protein levels and localization of the hepatic transcription factors in both cell types (Figure 1E). While FOXA1 and FOXA2 were translocated into the nuclei of iPSC-HLCs, they were expressed at low protein levels in Huh7 cells and homogenously distributed throughout the cytoplasm. Albumin expression was observed in both cell types (Figure 1E). We also compared the expression levels and localization of

Figure 1. iPSC-HLCs display molecular hepatic identity and retain hepatic functions

(A) Outline of the directed differentiation protocol used to generate iPSC-HLCs. SCT, STEMCELL Technologies; GFs, growth factors (fibroblast growth factor 2 [FGF-2], vascular endothelial growth factor [VEGF], epidermal growth factor [EGF]; Dex, dexamethasone; VK_1, vitamin K; OSM, oncostatin M.

(B) Representative flow cytometry analysis of five replicates of BU2 D0 and D5 iPSC differentiation into endoderm stained for definitive endoderm markers CXCR4 and c-kit (n = 5 independent replicates).

(C) Brightfield image of BU2 iPSC-HLCs at D23. Scale bar represents 200 μm.

(D) TaqMan qRT-PCR analysis of triplicate samples of three independent differentiations of BU2 iPSC-HLCs at D23, Huh7 cells, fetal liver, and adult liver (n = 3 technical replicates of three independent experiments for BU2; n = 3 technical replicates for all other cell types). Expression of each marker is normalized to β-actin and visualized as the fold change over D0 BU2 iPSCs. *AFP*, α-fetoprotein; *AAT*, alpha-1 antitrypsin protein; *FOXA1*, forkhead box A1; *FOXA2*, forkhead box A2; *HNF4α*, hepatocyte nuclear factor 4 alpha. Error bars represent SEM.

(E) Expression of albumin, FOXA1, and FOXA2, determined by immunofluorescence analysis in iPSC-HLCs (top row) and Huh7 cells (bottom row). Representative images of BU1 and BU2 and Huh7 samples (n = 1 from each donor for a total of two independent replicates per cell type). Images taken at 40× magnification or 63× magnification with oil, scale bars represent 20 μm. Albumin, BU2; FOXA1, BU1; FOXA2, BU1.

(F) Expression of HNF4α and transferrin, determined by duplicate immunofluorescence analysis of BU1 and BU2 iPSC-HLCs (top row), Huh7 cells (middle row), and donor A primary human hepatocytes PHHs (bottom row) (n = 1 technical replicate from each iPSC-HLC donor and n = 2 independent replicates for Huh7 cell samples and PHH donor A samples for a total of two independent replicates per cell type). Images taken at 40× magnification, 60× magnification, or 63× magnification with oil, scale bars represent 20 μm HNF4α, BU2; transferrin, BU2.

(G) Representative images of two replicates of low-density lipoprotein (LDL)-uptake assay for BU1 and BU2 iPSC-HLCs, Huh7 cells, and donor A PHHs (n = 2 technical replicates for each iPSC-HLC donor and cell type). LDL analog fluoresces red when endocytosed into the cell. Images taken at 10× (top row and bottom row, right image, scale bar represents 100 μm) or 40× magnification (bottom row, left and middle images, scale bar represents 20 μm). Cell nuclei were stained with DAPI; 10× magnification, BU2; 40× magnification, BU1.

(H) Representative PAS staining of three replicates of BU2 iPSC-HLCs, Huh7 cells, and donor A PHHs (n = 3 independent replicates per cell type). Images taken at 20× and 40× magnification, scale bar represents 100 μm.

(I) Detection of active CY3A4 in triplicate wells of a singular differentiation of BU2 iPSCs, BU2 iPSC-HLCs, and Huh7 cells using a P450-Glo assay (n = 3 independent replicates per cell type). Relative luciferase units (RLU) for each sample were normalized to RLU from supernatants of untreated cells. Error bars represent SEM of three technical replicates. ns, not significant; $***p \leq 0.001$; $****p \leq 0.0001$.

HNF4α and transferrin in iPSC-HLCs, PHHs, and Huh7 cells. Similar to FOXA1 and FOXA2, the transcription factor HNF4α was expressed at low levels and distributed homogenously in the cytoplasm of Huh7 cells, whereas it was localized in the nuclei of iPSC-HLCs and PHHs (Figure 1F). Transferrin, a clotting factor and carrier protein produced exclusively by hepatocytes in the liver, was robustly expressed in iPSC-HLCs and PHHs, but not in Huh7 cells (Figure 1F), further emphasizing the differences between the primary-like and immortalized cell platforms. Functional analysis of iPSC-HLCs and PHHs compared with Huh7 cells revealed major deficiencies in the Huh7 cells. One major function of hepatocytes *in vivo* is to store and metabolize lipoproteins, and an inability to bind or retain lipoproteins indicates a deficiency in hepatic function (Kwiterovich, 2000). While the majority of iPSC-HLCs and PHHs were positive in the low-density lipoprotein (LDL) uptake assay, LDL uptake was impaired in Huh7 cells (Figure 1G). Similarly, periodic acid-Schiff (PAS) staining, used to detect glycogen storage, resulted in the typical magenta staining in PHHs, whereas the Huh7 cells showed weak and diffuse staining (Figure 1H). PAS staining in iPSC-HLCs revealed bright pink-magenta staining, also indicating positive glycogen storage. Finally, we tested whether the iPSC-HLCs have proper cytochrome P450 function. Hepatocytes produce cytochrome P450 enzymes, which are involved in the metabolism of over 80% of all prescribed therapeutics (Ingelman-Sundberg et al., 2007). Immortalized hepatocytes express low levels of these enzymes unless specifically cultured in confluent conditions (Donato et al., 2013). To measure the enzymatic activity of the predominant cytochrome P450 enzyme, CY3A4, in iPSC-HLCs and Huh7 cells, we used a luminescent-based assay. In contrast to Huh7 cells that had no CY3A4 activity, iPSC-HLCs showed a strong luminescent signal indicative of CY3A4 enzymatic activity (Figure 1I).

It was previously reported that infection with vesicular stomatitis virus (VSV), a strong inducer of the type I IFN response, leads to type I IFN expression in PHHs but not in Huh7 cells (Marozin et al., 2008). To examine if the iPSC-HLCs were able to adequately respond to an acute viral infection, iPSC-HLCs and Huh7 cells were infected with VSV and *IFNB1* expression was analyzed by qRT-PCR. In contrast to Huh7 cells, *IFNB1* expression was strongly upregulated in infected iPSC-HLCs (Figure S1). This indicates that, similar to PHHs, iPSC-HLCs are IFN competent and able to respond to viral stimuli. It also confirms that Huh7 cells may not represent a suitable platform to analyze antiviral responses to viral infections.

Overall, these results indicate that iPSC-HLCs recapitulate functional and molecular hepatocyte features more faithfully than Huh7 cells do and therefore provide a better model to study EBOV hepatic infection.

iPSC-HLCs and PHHs support robust EBOV infection and replication

Next, we determined if iPSC-HLCs were permissive to EBOV infection. As a comparison, we also infected PHHs using a previously established platform based on cryopreserved adult primary hepatocytes collected from donors, allowing for the maintenance of primary hepatocytes in culture for up to several weeks (Khetani and Bhatia, 2008; March et al., 2015). We initially used micropatterned co-cultures (MPCCs) that consist of PHH islands supported by J2-3T3 murine embryonic fibroblasts. The MPCC system was successfully used to for hepatitis C and hepatitis B virus infection studies (March et al., 2015). However, despite robust EBOV infection of the PHHs in this co-culture system (Figures S2A and S2B), the MPCCs were less suitable for EBOV studies because the mouse fibroblasts were infected in addition to the PHHs, albeit at low infection rates (Figures S2A and S2B). Since the goal of this study was to dissect the host response of human hepatocytes to EBOV infection, infected mouse fibroblasts could potentially confound the results. Therefore, we took advantage of a controlled apoptosis system to remove the 3T3-J2s fibroblasts from the MPCCs prior to infection (Chen et al., 2020).

iPSC-HLCs from three different donors (BU1–3), PHHs from two donors in fibroblast-depleted MPCCs, and Huh7 cells were infected with EBOV over a time course of 7 days and analyzed by immunofluorescence staining. At 1 day post infection (dpi), about 50% of iPSC-HLCs and PHHs were infected and about 90% of the Huh7 cells (Figure 2A). Viral inclusion formation, a hallmark of EBOV infection, was observed in all three cell types (Figure 2B). In parallel, we collected supernatants from the infected cells to determine viral titers over the course of infection. Viral titers peaked at 3 dpi, with the highest titers produced in Huh7 cells (5×10^5) followed by iPSC-HLCs (2×10^4) (Figure 2C). The increase in viral titers correlated with an increase in the percentage of infected cells in culture, which consistently showed 80%–90% infection by 3 dpi (Figure 2A). Infected PHHs showed a modest increase in viral production and PHHs over time with overall lower titers (1×10^3) compared with the iPSC-HLCs. In summary, these data show that iPSC-HLCs and PHHs are permissive to EBOV infection and that iPSC-HLCs support EBOV replication more efficiently than PHHs do.

Since the iPSC-HLCs showed robust EBOV infection, we focused on this cell type for a more phenotypical characterization. To visualize spatial and temporal viral RNA production in infected cells at early and late time points, we performed single-cell, single-molecule fluorescent RNA *in situ* hybridization (RNA-FISH) using RNAscope technology.

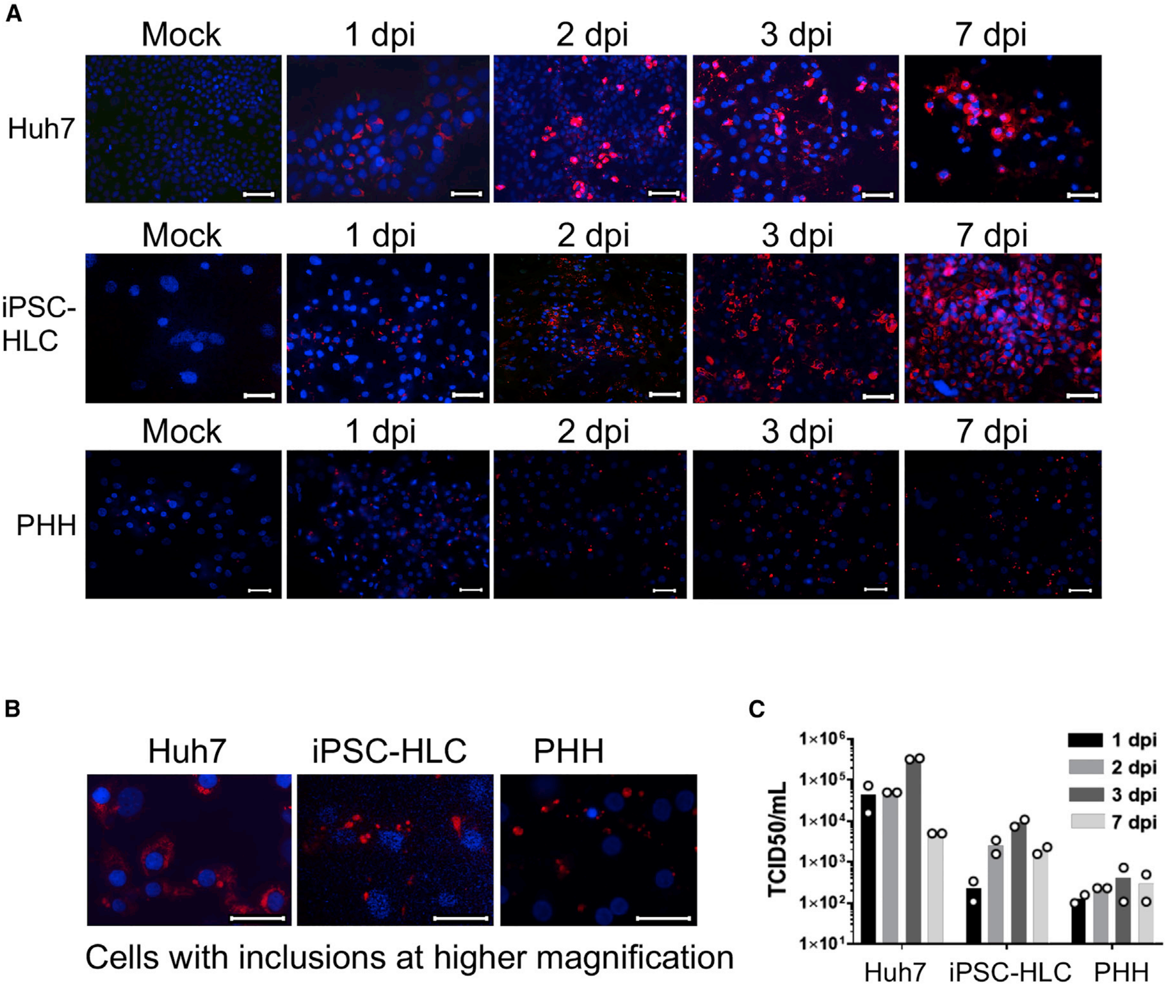

Figure 2. iPSC-HLCs and PHH are susceptible to EBOV infection

(A) Immunofluorescence analysis of EBOV-infected Huh7 cells, BU2 iPSC-HLCs, and donor A PHHs. Cells were mock infected or infected with EBOV at an MOI of 10, fixed at the indicated time points, and stained with an antibody directed against EBOV nucleoprotein (red). Cell nuclei were stained with DAPI. Images are representative of triplicate replicates (n = 3 technical replicates per cell type). Images of iPSC-HLCs and Huh7 cells taken at 40× magnification. Images of PHHs taken at 20× magnification. Scale bar represents 20 μm.

(B) Higher magnification to visualize viral inclusions. Images taken at 63× magnification. Scale bar represents 20 μm.

(C) Viral titers of each EBOV-infected hepatocyte platform at the indicated time points. Bars represent the average of two technical replicates (n = 2 technical replicates per cell type). iPSC-HLCs, BU2; PHH, donor A.

The used probes are directed against EBOV *VP35* positive-sense RNA, which includes *VP35* mRNA and antigenomic RNA. Robust viral mRNA production was observed at 8 h post infection (hpi) with a punctate staining pattern throughout the cytoplasm, each small dot likely representing a single mRNA molecule, whereas larger bright puncta may represent RNA aggregates (Figure 3A). At 2 dpi, the viral RNA was homogenously distributed throughout the cytoplasm and aggregated in clusters that co-localize with viral inclusions.

Electron microscopy (EM) analysis of EBOV-infected iPSC-HLCs confirmed the formation of EBOV nucleocapsids in the cytoplasm of the infected cells and the release of viral particles (Figure 3B). Newly synthesized EBOV nucleocapsids accumulated in viral inclusions and were arranged in parallel tubes in a hexagonal pattern in which each nucleocapsid is surrounded by six neighboring nucleocapsids, in line with previously reported observations (Figure 3C) (Kolesnikova et al., 2017). The accumulation of viral inclusions and the release of viral particles was observed at 1 and 2 dpi for all three donors (Figures 3D–3F).

To follow the course of EBOV infection in iPSC-HLCs by live cell imaging, we used a recombinant EBOV clone

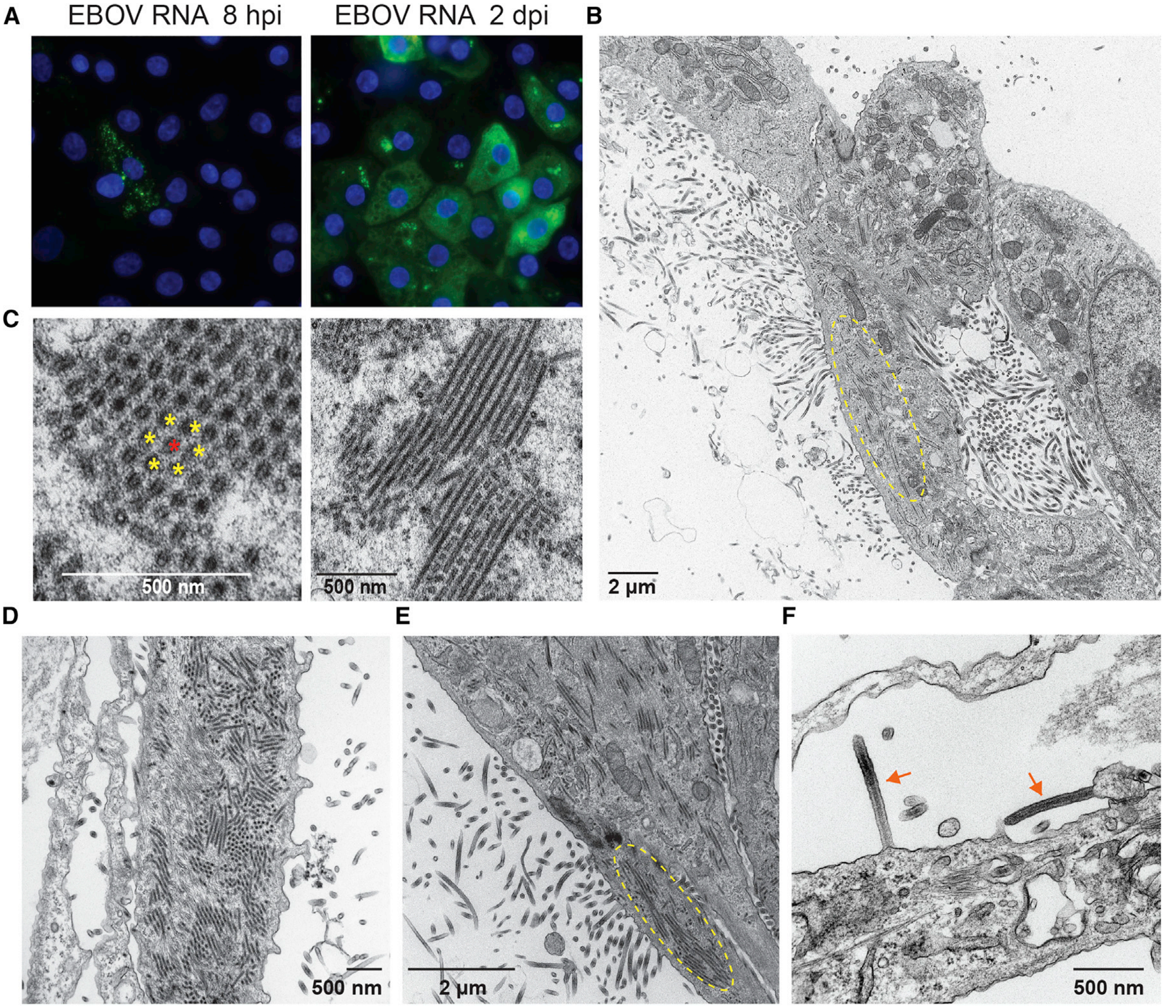

Figure 3. Productive EBOV infection of iPSC-HLCs

(A) RNA-FISH analysis of BU2 EBOV-infected iPSC-HLCs at the indicated time points using probes directed against EBOV *VP35* mRNA. Scale bar represents 20 µm. Images are representative of BU1, BU2, and BU3 samples (n = 1 technical replicate per iPSC donor per time point for a total of three independent replicates per time point).

(B–F) Transmission electron microscopy of BU2 EBOV-infected iPSC-HLCs at 1 and 2 dpi. Cells were infected with an MOI of 3. Image is representative of infections in BU1, BU2, and BU3 (n = 1 replicates per iPSC donor per time point for a total of three independent replicates per time point). (B) Overview of BU2 EBOV-infected cell at 2 dpi. Circled area indicates the accumulation of filamentous viral nucleocapsids into inclusions. (C) Higher magnification of cross-sectioned (left) and longitudinal sectioned (right) viral inclusions. Single nucleocapsids are marked with yellow and red asterisks, respectively, to visualize the hexagonal pattern. (D and E) Release of viral particles at 1 dpi (D) and 2 dpi (E). Circled area in (E) indicates viral inclusions. (F) Arrows indicate mature, budding Ebola virions. Cells were fixed at 2 dpi. Images were taken from cells derived from different donors: (A–D) donor BU2, (E) donor BU1, (F) donor BU3.

expressing green fluorescence protein (GFP) from an additional transcription unit (Towner et al., 2005). Although the cells were infected with a high MOI of 10, we observed peak infection only at 3 dpi (Figure S3). At 7 dpi, the infected cells showed a pronounced cytopathic effect (CPE), leading to reduced GFP expression. Overall, these data indicate that iPSC-HLCs can be productively infected with EBOV and that the infection leads to cell damage at late time points.

EBOV infection induces a delayed type I IFN response in human hepatocytes

To analyze the transcriptional profile induced by EBOV infection across the three infection platforms, iPSC-HLCs, PHHs, and Huh7 cells were infected with purified Ebola virions, and the cellular RNA was harvested 24 hpi for bulk RNA sequencing analysis. The chosen time point was based on the transcriptional response to EBOV infection in human monocyte-derived macrophages, which display a strong transcriptional signature at 24 hpi (Olejnik et al., 2017). We calculated the log fold change (logFC) in expression for each aligned transcript between the EBOV-infected sample and mock control to determine which transcripts were differentially expressed for each condition and ranked these genes based on absolute logFC. However, our results indicated that there was no significant differential gene expression in infected compared with non-infected cells in either cell type (Figure S4).

Since we observed peak infection of EBOV-infected iPSC-HLCs as late as 3 dpi (Figure S3), this inspired us to explore the transcriptional response to EBOV infection in liver cells at later time points. iPSC-HLCs were infected with EBOV and cellular RNA was isolated at 1, 2, 3, and 7 dpi for bulk transcriptomics analysis. Principal component analysis (PCA) of mock-infected compared with EBOV-infected samples at all time points showed clear clustering of the replicates, separating the non-infected from the infected samples at each time point, particularly at 2, 3, and 7 dpi (Figure 4A). We observed minimal gene expression changes at 1 dpi, confirming our previous RNA sequencing data. When we ranked the differentially expressed genes based on the false discovery rate (FDR)-corrected p value, there were only 20 upregulated genes and 14 downregulated genes with an adjusted p value ≤ 0.01 at 1 dpi (Table S1). We then applied the same analysis across all time points in mock-infected and EBOV-infected iPSC-HLCs over time and plotted the 250 most variable genes as a heatmap (Figure 4B). Clear gene expression signatures related to EBOV infection emerge at 2 and 3 dpi, converging into a different signature by 7 dpi. Starting 2 dpi, we observed a pronounced type I and III IFN signature, specifically upregulation of *IFNB1*, *IFNL1-3*, and a set of IFN-stimulated genes (ISGs). There was a strong overlap of the top 30 differentially expressed genes (DEGs) at 2 and 3 dpi (20 out of 30), including 13 ISGs (Figures 4B, 4C, and S5A). To further assess the induction of a type I/III IFN response in EBOV-infected cells, we plotted the fold change of a panel of type I/III IFNs and 50 ISGs for each time point, confirming the upregulation of ISGs at 2 dpi and, even more pronounced, 3 dpi, including *IFNL1-3*, *IFNB1*, chemokine ligand 5 (*CCL5*), 2′-5′-oligoadenylate synthetase like (*OASL*), *OAS1*, interferon-induced protein with tetratricopeptide repeats 1 (*IFIT1*), *IFIT2*, and the poorly characterized interferon-induced protein 44 (*IFI44*), which was shown to have antiviral activity (Busse et al., 2020; Carlton-Smith and Elliott, 2012; Power et al., 2015) (Figure 4C). By 7 dpi, the IFN response signature was no longer present (Figure 4C). To confirm that we observe similar antiviral responses within 2–3 dpi across multiple donors, we assessed the expression of *CXCL10*, *CCL5*, and *ISG15* by qRT-PCR at each time point in EBOV-infected HLCs from multiple donors (Figure S5C). While we observed variations in gene expression for each donor, the expression of each of these ISGs peaked between 2 and 3 dpi for each donor, confirming that this time point is critical for the initiation of antiviral responses in EBOV-infected HLCs (Figure S5C).

A striking feature of the host response signature in the infected iPSC-HLCs was a general downregulation of genes at later time points, many of them associated with characteristic liver functions. For instance, several of the downregulated genes were associated with aminotransferases and ion transport (9 of 30 genes) (Figure S5B). *AGXT*, cytochrome P450 enzyme *CYP3A7*, the bile acid transporter nuclear receptor subfamily 1 group H member 4 (*NRIH4*), *SERPINA7*, *ITIH1*, and *ITIH3* were all significantly downregulated at 7 dpi (Figure S5B). Genes involved in plasma formation and clotting, including *ALB*, insulin-like growth factor 2 (*IGF2*), podocan (*PODN*), and n-acetyltransferase 16 (*NAT16*), were also downregulated at this time point (4 of 30) (Figure S5B). We further confirmed the significant downregulation of liver-associated genes in EBOV-infected iPSC-HLCs 3 dpi by using a curated list of liver-specific genes for comparison (Wilson et al., 2015), including albumin (*ALB*), serpina genes (*SERPINA 1* and *SERPINA 3*), fibrinogen genes (*FGA*, *FGB*, and *FGG*), apolipoprotein genes (*APOA1*, *APOA2*, and *APOC1*), and angiopoietin (*ANG*) (Figure 4D). To determine if the downregulation of these genes at later time points was due to EBOV-induced apoptosis, we analyzed cells for caspase 3 activity using a luminescent assay (Figure S7). There was minimal CPE in EBOV-infected HLCs and Huh7 cells and minimal caspase activity compared with staurosporine-treated control cells (Figures S7A and S7B), indicating that EBOV did not induce apoptosis in the infected cells. Overall, our data suggest that EBOV infection leads to severe liver cell damage associated with loss of hepatic functions.

To identify pathways that were perturbed during EBOV infection, we performed gene set enrichment analysis (GSEA) on the DEGs in EBOV-infected cells compared with mock-infected controls, using WebGestalt (Liao et al., 2019). Gene ontology (GO) analysis showed moderate upregulation of IFN response pathways in EBOV-infected cells at 2 and 3 dpi (Figure 5). Hallmark pathway analysis confirmed these results, highlighting that the IFNα response pathway is upregulated at 2 and 3 dpi (Table S2). Importantly, there was no upregulation of inflammatory response pathways, suggesting that EBOV infection does not trigger a proinflammatory response in primary-like hepatocytes. While there were only few moderately upregulated pathways in EBOV-infected cells, pathway downregulation was more pronounced over the course of infection, which we observed in the DEG profile. This includes pathways related to metabolic processing, protein synthesis, protein transport, protein membrane localization, and extracellular structure organization,

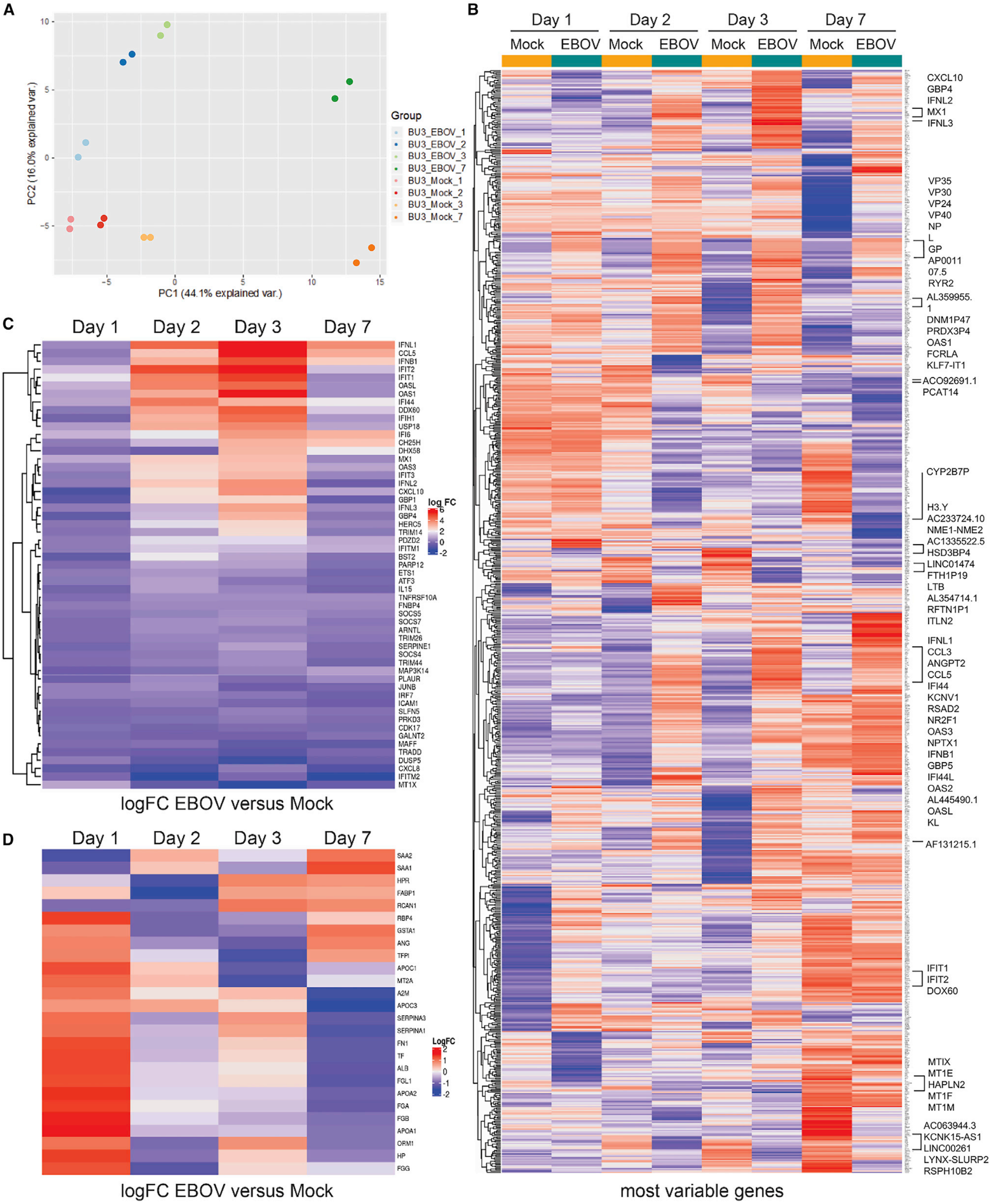

(legend on next page)

indicating cellular shutdown (Figure 5). By hallmark pathway analysis, there were no upregulated pathways at 7 dpi (Table S2). By GO analysis, responses to type I IFN and response to virus were slightly upregulated at 7 dpi, which we hypothesize is driven by the low expression of *IFNB1* and *IFNL1-3* at this time point (Figures 4 and 5). Hallmark pathway analysis suggested a downregulation of coagulation and xenobiotic metabolism pathways, indicating that EBOV-infected hepatocytes respond with a reduced capacity to produce clotting factors or metabolize drugs, which are suggested implications of liver damage during EBOV infection of NHPs (Table S2) (Geisbert et al., 2003c, 2003d). This analysis highlights the changing dynamics in the host response of EBOV-infected iPSC-HLCs.

IFNB1 and *CXCL10* expression in EBOV-infected iPSC-HLCs is delayed and mainly observed in non-infected bystander cells

Bulk RNA analysis only provides the average gene expression levels of a diverse cell population and does not allow us to discriminate between the host response signatures in infected and non-infected cells. Given the clear but moderate type I/III IFN response in EBOV-infected iPSC-HLCs, we hypothesized that there might be significant heterogeneity regarding the IFN response in this cell population. To assess the IFN and inflammatory response at single-cell level, we performed RNA-FISH analysis with infected iPSC-HLCs using probes targeting *IFNB1*, *CXCL10*, and *IL6* mRNA in combination with EBOV-specific probes targeting *VP35* mRNA. The number of the cells with detectable *VP35* expression increased from about 20% at 1 dpi to 60%–70% at 2 and 3 dpi (Figures 6A and 6B). Consistent with the RNA sequencing data, less than 2% of the cells expressed *CXCL10* (1.6%) or *IFNB1* (0.2%) at 1 dpi (Figures 6A, 6C, and 6D). We observed an increase in both *CXCL10*- and *IFNB1*-expressing cells at 2 and 3 dpi with up to 2% of *IFNB1* and 6% of *CXCL10*-expressing cells. Luminex analysis confirmed the secretion of CXCL10 in the supernatants of infected cells (Figure S6D). Of note, *CXCL10* and *IFNB1* were mainly expressed in uninfected bystander cells. The ratio of uninfected to infected *IFNB1*-expressing cells increased from 50% at day 1 to 92% at day 3 (Figure S6A). The signal intensity of EBOV mRNA was weak in cells expressing *IFNB1* or *CXCL10*, suggesting that these cells represent early stages of infection with low expression rates of VP35 and VP24, the known EBOV IFN antagonists. There was no detectable *IL6* expression in infected iPSC-HLCs at any time point post infection, confirming the absence of an inflammatory response in these cells (Figure S6B). In contrast to the iPSC-HLCs, we did not observe *IFNB1* or *CXCL10* expression in Huh7 cells (Figure S6C). This is in line with previous studies using immortalized hepatocytes that did not observe a delayed IFN response upon EBOV infection (Hartman et al., 2008; Kuzmin et al., 2017). Overall, the RNA-FISH results corroborate the findings from the transcriptomic analysis and suggest that EBOV infection of iPSC-HLCs induces a delayed and moderate type I IFN response that is not observed in infected Huh7 cells.

EBOV can be transmitted from infected macrophages to iPSC-HLCs

Since there is evidence that migrating monocytes or tissue-resident macrophages are early target cells in the liver (Geisbert et al., 2003b; Greenberg et al., 2020), we explored whether EBOV can be transmitted from infected macrophages to iPSC-HLCs in a co-culture model. Donor-matched human primary monocyte-derived macrophages (MDMs) were infected with recombinant EBOV expressing GFP at an MOI of 10 to ensure that all MDMs were EBOV infected. At 1 dpi, the infected MDMs were detached, rigorously washed, and seeded onto iPSC-HLCs. Spread of infection was visualized by GFP expression (Figure 7). While only single green cells were observed at 2 dpi, likely representing the infected MDMs, the infection spread throughout the entire iPSC-HLC monolayer over the time course of 7 days, indicating that EBOV infection of hepatocytes can be initiated by infected macrophages.

DISCUSSION

Although the liver plays a crucial role in EBOV disease, the intrinsic response of human hepatocytes to EBOV infection is not well defined. *In vitro* hepatocyte platforms are limited

Figure 4. Upregulation of ISGs and downregulation of genes involved in liver function in EBOV-infected iPSC-HLCs at 2 and 3 dpi

(A) Principal component analysis (PCA) of transcriptional responses of EBOV- and mock-infected BU3 iPSC-HLCs at each time point (n = 2 technical replicates per infection condition per time point). PCA1 represents the majority of variance and is associated with the day of differentiation. PCA2 represents the second largest contributor of variance and is associated with infection status.

(B) Heatmap displaying the 250 most variable genes at each time point. Highlighted are the top 30 upregulated and downregulated DEG at 3 dpi. Key for the value of the logFC to the right of the plot.

(C) Heatmap displaying the logFC for a list of ISGs (right of the plot) of EBOV-infected iPSC-HLCs compared with mock-infected cells at the indicated time points. Key logFC change in expression shown to the right.

(D) Heatmap displaying the logFC for a list of genes involved in liver function (right of the plot) of mock- and EBOV-infected iPSC-HLCs at 3 dpi. Shown are the technical replicates for each condition. Key logFC change in expression shown to the right.

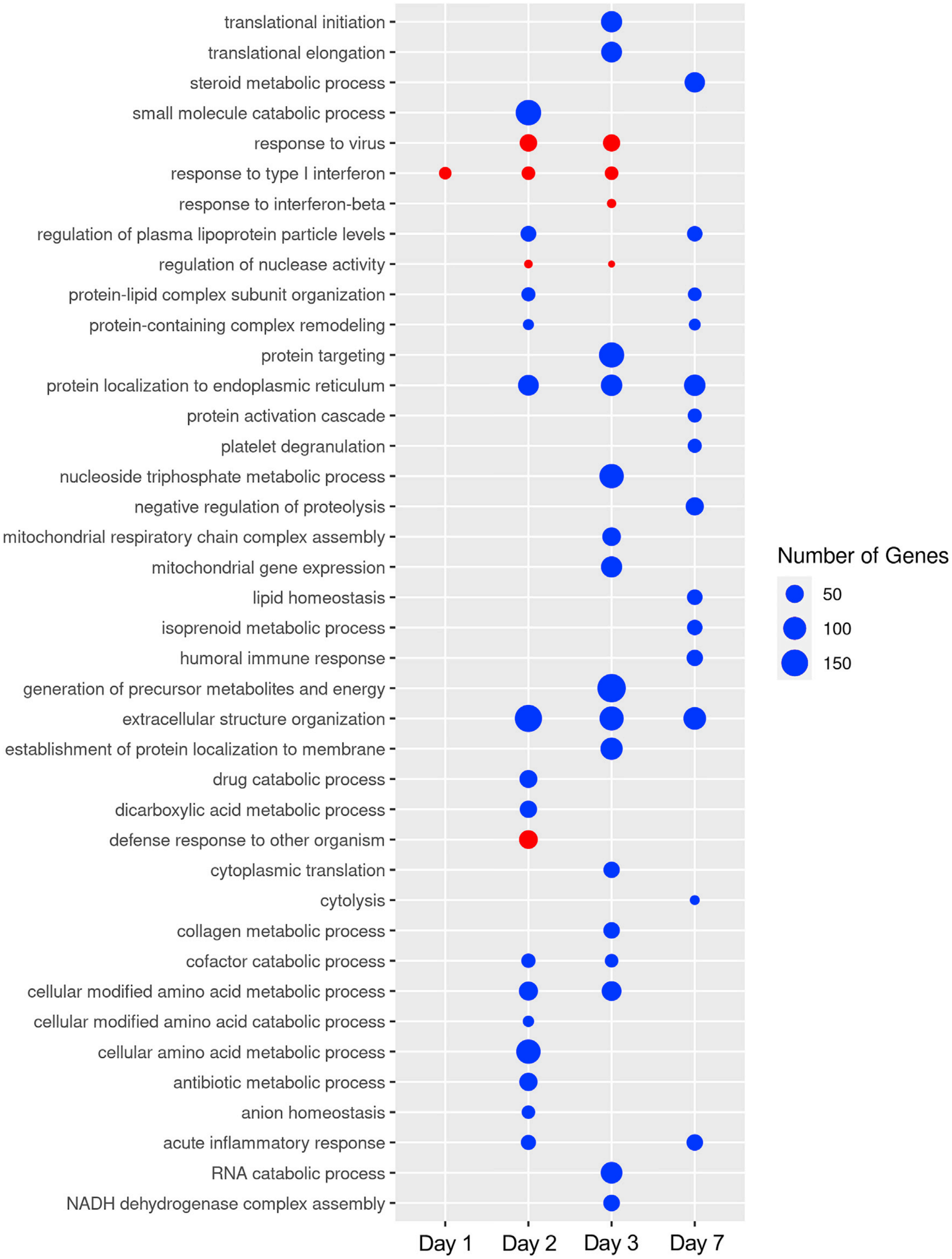

Figure 5. EBOV infection of iPSC-HLCs leads to a general downregulation of critical pathways with the exception of viral response pathways

Gene Ontology (GO) analysis of the DEGs in EBOV- compared with mock-infected BU3 iPSC-HLCs for each time point (n = 2 technical replicates per infection condition per time point). FDR ≤0.01. Time point labeled on the bottom of the plot, GO pathways labeled on the

(legend continued on next page)

in their capacity to recapitulate human immune responses. Immortalized hepatocytes like Huh7 cells have impaired IRF3 signaling (Marozin et al., 2008), which our study highlights as an important signaling cascade in the EBOV-induced hepatic host response. Additionally, immortalized cell lines can vary significantly from lot to lot, preventing an accurate comparison of results across studies, even within the same cell line (Ben-David et al., 2018). PHHs are difficult to culture and require intricately engineered culture systems to support *in vitro* survival (Khetani and Bhatia, 2008; March et al., 2015; Xiang et al., 2019). In the co-culture system presented in this study, PHHs destabilize 2 to 3 days after the removal of the fibroblast stroma, which challenges the use of this PHH culture system for longer infection times (Chen et al., 2020). There are recent studies that utilize a combination of small molecules to maintain stable PHHs in culture for up to 4 weeks, which could allow for longitudinal EBOV infections to be performed on a primary hepatocyte (Xiang et al., 2019). However, these culture systems still require delicate engineering to maintain their function. Additionally, all PHH systems are dependent on donor cell availability, which can limit the genetic backgrounds or diversity of samples used in immune response studies. For these reasons, we used iPSC-HLCs as an alternative to traditional immortalized and primary culture models. We have demonstrated that iPSC-HLCs are terminally differentiated hepatocytes and primary-like in their functional capacity. iPSC-HLCs are also differentiated as a monoculture that can be sustained in a functional state for 10 days, allowing for longer infection studies than PHH culture systems. iPSC-based platforms also offer additional advantages, such as the ability to differentiate into multiple cell types from one donor to create organ-specific co-culture systems within one genetic background. This advantage is applicable to EBOV pathogenesis studies since EBOV infects many different cell types and organs, which may contribute to disease progression.

Using the iPSC-based platform, we began to define the intrinsic hepatic response to EBOV infection. The most prominent transcriptional changes are defined by the downregulation of pathways involved in critical cellular processes later in infection, such as protein production and transport, and extracellular structure organization. This general shutdown of cell function is contrasted by a moderate upregulation of type I and type III IFN responses dominated by the expression of *IFNB1*, *IFNL1*, and select ISGs beginning 2 dpi and increasing at 3 dpi. At single-cell level, *IFNB1* and *CXCL10* expression was observed in uninfected bystander cells and cells with low expression levels of EBOV mRNA. This is in line with RNA-FISH analysis on liver samples obtained from EBOV-infected NHPs, showing *ISG15* expression predominantly in uninfected bystander cells (Greenberg et al., 2020). In addition, single-cell analysis of blood from EBOV-infected NHPs and infected human peripheral blood mononuclear cells revealed that ISG expression is mainly elicited in uninfected bystander monocytes or monocytes with low amounts of viral RNA, corroborating our results. Although EBOV generally suppresses type I IFN induction in the infected cells (Kotliar et al., 2020; McElroy et al., 2018), there is a strong proinflammatory response in EVD patients and infected animals associated with specialized immune cells, including macrophages and monocytes (Caballero et al., 2016; Greenberg et al., 2020; Kotliar et al., 2020; Liu et al., 2017; McElroy et al., 2016). In contrast to monocytes and macrophages, there was no induction of a proinflammatory response in EBOV-infected human iPSC-HLCs, indicating that, indeed, immune cells are the main drivers of EBOV-induced inflammation. Of note, iPSC-HLCs have been shown to be able to respond to exogenous stimuli by mounting an inflammatory signature, indicating that the lack of an inflammatory response in EBOV-infected cells is not due to the inability of the cells to induce inflammatory cytokines (Fischer et al., 2020).

A crucial question that still needs to be addressed from our observations is that hepatocytes are consistently silent 1 dpi, despite significant infection at this time point. This delayed antiviral response might provide an environment that favors undisturbed viral propagation and open a window for early therapeutic intervention through stimulating an antiviral response by inducing IFN production in uninfected bystander cells. Indeed, US Food and Drug Administration (FDA)-approved therapeutics that stimulate antiviral responses have been shown to inhibit EBOV infection in immortalized cell culture systems and could be tested using the primary-like platform described in this study (Jasenosky et al., 2019).

Another critical component of the hepatic response to EBOV infection is the downregulation of coagulation and acute-phase reactant pathways beginning 2 dpi. Coagulopathy is a well-established clinical indicator of severe EBOV infection, although the exact impact of consumptive coagulopathy on the pathogenesis of EVD is poorly understood (Feldmann and Geisbert, 2011). In our study, iPSC-HLCs downregulated the coagulation cascade 2–7 dpi. We did not observe an increase in acute-phase reactants that has been observed in NHPs (Ward et al., 2019). Our data indicate downregulation of critical clotting factors and plasma proteins, including ALB; fibrinogen chains alpha, beta, and

left of the plot, key located on the right of the plot. Red bubbles mark pathways that are upregulated at each time point, and blue bubbles denote pathways that are downregulated at each time point. The GO analysis by WebGestalt determined that all p values = 0, indicating that the p value is <0.001 for each pathway.

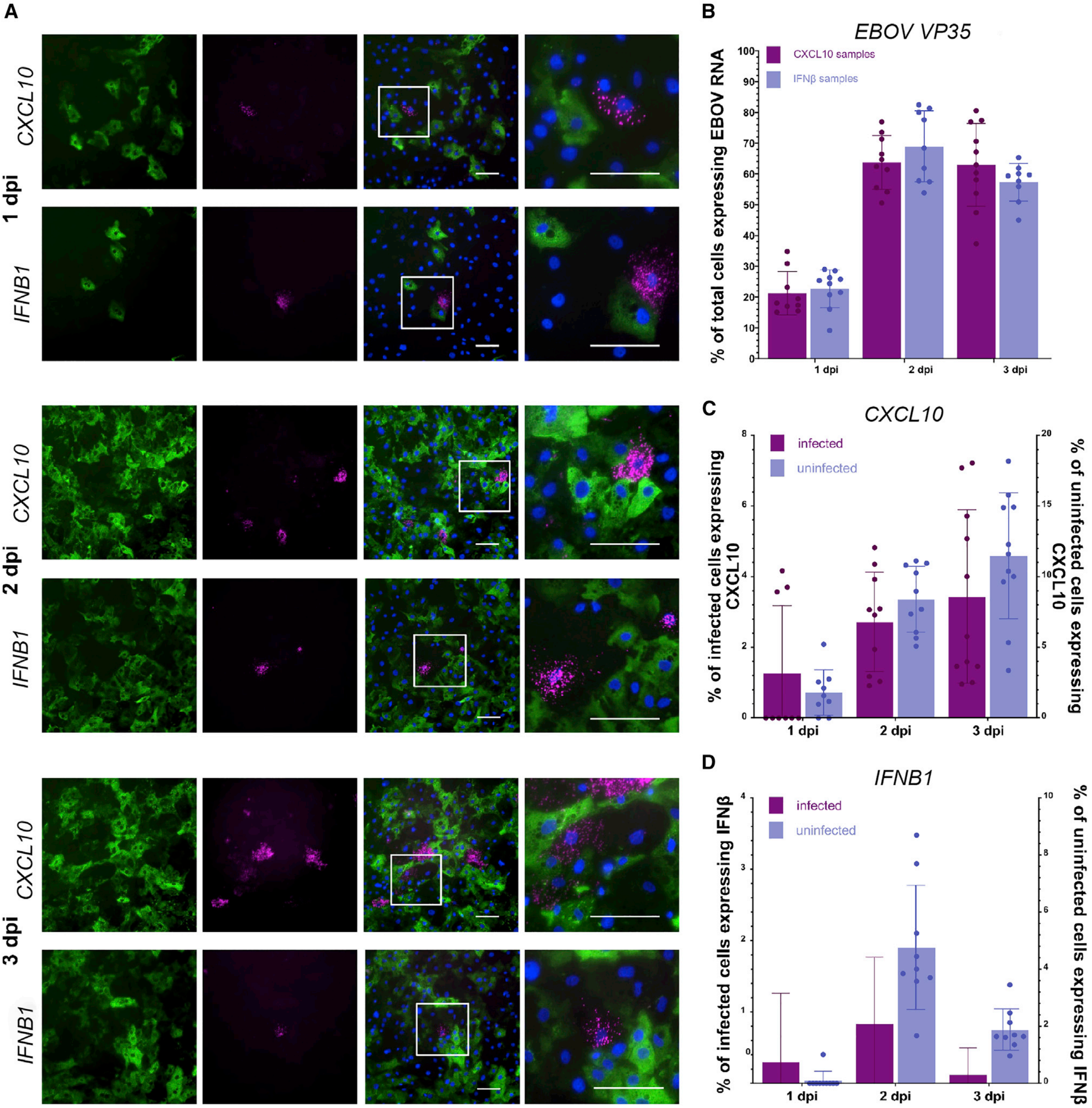

Figure 6. RNA-FISH analysis reveals expression of IFNB1 and CXCL10 in uninfected bystander cells and cells with weak EBOV mRNA signal intensity

(A) EBOV-infected BU1 and BU2 iPSC-HLCs were fixed at the indicated times and analyzed by RNA-FISH using a combination of probes against EBOV *VP35* mRNA (green) and *CXCL10* (magenta, top row), or *IFNB1* (IFNβ, magenta, bottom row) mRNA. Shown are representative images from both donors at each time point at 20× magnification, and right column shows inset region of merged images (n = 2 technical replicates per iPSC donor per time point for a total of four replicates per time point; two technical replicates of two different donors). Scale bars represent 100 μm.

(B–D) Quantification of gene expression from images using at least 1,200 cells and eight fields of view per time point and probe combination. (B) Percentage of total cells positive for EBOV *VP35* mRNA at each time point. Error bars represent SD. (C) Percentage of infected

(legend continued on next page)

gamma (FGA, FGB, and FGG); protein c (PROC); and F3 as early as 2 dpi. This discrepancy could be evidence of a compensatory feedback loop designed to prevent coagulation dysfunction or consumptive coagulopathy. Fibrinogen levels are lower in EBOV patients than healthy controls and increase in patients who survive, and low levels of serum ALB is a hallmark indicator of EBOV-induced liver damage in NHPs (Geisbert et al., 2003a; Smither et al., 2019). This is emphasized by the network analysis of the 7 dpi DEG that highlighted HNF1A as a critical regulator of the gene expression profile. In EBOV-infected NHPs, another hepatic nuclear factor homeobox gene (HNF4A) was significantly downregulated in the liver, and the authors attributed the downregulation of this transcription factor with the associated downregulation of genes involved in cholesterol synthesis, coagulation, and hepatic metabolism (Jankeel et al., 2020). HNF1A is known to regulate the expression of HNF4A, which may highlight overlap in the transcriptional signatures between our EBOV-infected iPSC-HLCs and bulk NHP liver tissue (Boj et al., 2001; Jankeel et al., 2020). Of the HNF4A targets listed in this study as downregulated transcripts in the liver, we observed significant downregulation in 11 of 17 genes (*PCK2*, *PDK4*, *APOB*, *CYP3A7*, *CYP2A6*, *F7*, *TF*, *F3*, *TTR*, and *SERPINC1*) (Jankeel et al., 2020). Clearly, the expression of coagulation factors in hepatocytes is affected during EBOV infection, but the role that this may play in pathogenesis, organ failure, or patient outcome is poorly understood. This platform allows for further investigation of the hepatic responses to EBOV infection that can help elucidate the complex mechanisms that underlie liver pathology infection.

The use of co-culture systems, such as the one highlighted in this study, can help determine which cell types in the liver are responsible for specific host responses, helping to define a cell-intrinsic disease signature that is difficult to discern in the whole-organ environment. The data presented here corroborate that genes associated with liver function are perturbed in EBOV-infected hepatocytes. Future studies using this platform can help identify how EBOV impairs liver function during disease progression and inform the development of therapeutic interventions that may universally prevent EBOV fatality.

EXPERIMENTAL PROCEDURES

iPSC culture and directed differentiation into hepatocytes

iPSC lines used in this study were BU1, BU2, and BU3. iPSCs were generated and characterized as previously described (Park et al., 2017). Briefly, reprogramming of peripheral blood was done with the STEMCCA reprogramming vector (Somers et al., 2010) and, upon reprogramming, the reprogramming cassette was excised.

iPSCs were maintained on Matrigel-coated six-well tissue culture plates in 2 mL of mTeSR 1 feeder-free medium (STEMCELL Technologies) with 200 ng/mL Primocin (Invitrogen). The directed differentiation from iPSCs into hepatocytes was performed as previously described (Wilson et al., 2015). iPSCs were seeded onto Matrigel-coated six-well tissue culture plates with 2 mL of mTeSR feeder-free medium. For D1–D5 of the differentiation protocol, the STEMdiff Definitive Endoderm kit (STEMCELL Technologies) was used according to manufacturer's instructions. At D5, iPSC-derived endoderm cells were split at a 1:4 or 1:5 ratio, depending on the iPSC line, and differentiated into HLCs following the schedule and cytokine concentrations outlined in Table S4. The culture medium was changed on D5 and D6. From D7 until the start of each experiment, the culture medium was changed every other day. At D19, the cells were terminally differentiated, and cells were used for experiments between D19 and D26. From D0 until the day of infection, the cells were incubated in a hypoxic incubator at 37°C. During infection, cells were incubated in normoxic conditions.

Primary hepatocyte cell culture

The PHH co-culture with murine embryonic fibroblasts 3T3-J2s were generated by seeding cryopreserved primary human hepatocytes purchased from BioIVT on collagen-patterned 96-well plates as described previously (Khetani and Bhatia, 2008; March et al., 2015). 3T3-J2s were a kind gift provided by Howard Green, Harvard Medical School. Fibroblast-depleted micropatterned PHH cultures were obtained by incorporation of 3T3-J2s expressing an inducible apoptosis switch (inducible caspase-9 [Casp9]). 3T3-J2s were lentivirally transduced with the pMSCV-F-del Casp9.IRES.GFP plasmid (15567, Addgene) followed by FACS purification (top 15%, FACSAria II, BD Biosciences) (Chen et al., 2020). On the day of infection, PHH co-cultures were dosed with a chemical inducer of dimerization (0.5 μM AP20187, Takarabio) to trigger fibroblast removal via apoptosis. PHH co-cultures were maintained in Dulbecco's modified Eagle's medium (DMEM, Corning) supplemented with 10% fetal bovine serum (Gibco), 1% insulin/transferrin/selenous acid and linoleic acid (ITS; BD Biosciences), 7 ng/mL glucagon (Sigma-Aldrich), 40 ng/mL dexamethasone (Sigma-Aldrich), 15 mM HEPES (Gibco), and 100 μg/mL penicillin-streptomycin (Corning). Cells were kept at 37C with 5% CO_2. Donors utilized in this study are labeled as donor A and donor B.

Virus infection and purification

Work with infectious EBOV was performed at Boston University's National Emerging Infectious Diseases Laboratories, Boston, MA and at the NIH/NIAID Integrated Research Facility, Fort Detrick, MD. EBOV isolate Mayinga (GenBank: AF086833.2; kindly provided by H. Feldmann, NIH NIAID Rocky Mountain Laboratories, Hamilton, MT) and recombinant EBOV-GFP (Mayinga isolate;

cells expressing *CXCL10* mRNA, left axis, and percentage of uninfected cells expressing *CXCL10* mRNA, right axis. Error bars represent SD. (D) Percentage of infected cells expressing *IFNB1* mRNA, left axis, and percentage of uninfected cells expressing *IFNB1* mRNA, right axis. Error bars represent SD. (A) Upper, BU2; lower, BU2. (B) Upper, BU1; lower, BU1. (C) Upper, BU1; lower, BU1.

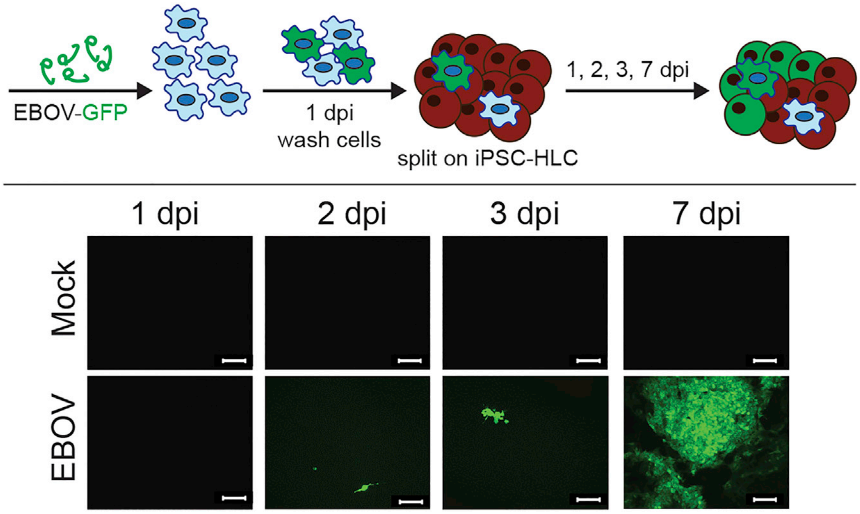

Figure 7. Transmission of EBOV-GFP from monocyte-derived macrophages (MDMs) to iPSC-HLCs

Top, infection scheme and workflow. Bottom, live fluorescent imaging of BU2 MDM and BU2 iPSC-HLC co-cultures; 10× magnification. Images taken from one well over the period of 1–7 dpi. Scale bar represents 20 μm. Images are representative of two independent experiments performed with BU1, BU2, and BU3 (n = 1 per iPSC donor at each time point for a total of three independent replicates per time point for each infection. This infection time course was performed twice for a total of six independent replicates per time point).

kindly provided by the World Reference Center for Emerging Viruses and Arboviruses, University of Texas Medical Branch, Galveston, TX) expressing GFP from an additional transcription unit (Towner et al., 2005) were propagated in Vero E6 cells as described before (Olejnik et al., 2017). Cell supernatants were centrifuged at 1,000 × g for 10 min at 4 °C to remove cellular debris. Clarified supernatants were purified over a 20% sucrose cushion by centrifugation at 25,000 rpm for 2 h at 4 °C and viral pellets were resuspended in PBS. Viral titers were determined by tissue culture infectious dose 50 ($TCID_{50}$) assays and focus forming unit (FFU) assays as previously described (Olejnik et al., 2017). All EBOV infection studies were performed with purified virions. If not stated otherwise, cells were infected at an MOI of 10. After addition of the inoculum, virions were allowed to adsorb for 20 min to 1 h at 37°C before cells were washed and fresh cell culture medium was added.

qRT-PCR and RNA sequencing

Cells were harvested for RNA analysis by using either the RNeasy Kit (Qiagen) or TRIzol Reagent (Thermo Fisher) according to manufacturer's instructions. Detailed descriptions of qRT-PCR analysis, Illumina sequencing, and SmartSeq2 sequencing, including data analysis, are provided in the supplemental methods.

Immunofluorescence analysis

Cells were fixed with either 4% PFA or 10% formalin and permeabilized with acetone-methanol. Primary antibody names and dilutions are listed in Table S3. A detailed description of the procedures is provided in the supplemental methods.

Fluorescence *in situ* hybridization assay

Fluorescence *in situ* hybridization (RNA-FISH) was performed using the Advanced Cell Diagnostics RNAscope v2 kit according to manufacturer's instructions (ACD Bio) and as previously described (Hume et al., 2022). A detailed protocol is provided in the supplemental methods. The following probes (all from ACD Bio) were used: ebolavirus Zaire VP35-C1, human IL6-C2, human IFNβ-C3, and human CXCL10-C3.

EM

For conventional thin-section microscopic evaluation, 4 × 10^5 EBOV-infected BU1, BU2, and BU3 iPSC-HLCs were inactivated and preserved in 2.5% glutaraldehyde (E.M. Sciences, Warrington, PA), in Millonig's sodium phosphate buffer (Tousimis Research, Rockville, MD), for 24 h (n = 1 for each donor at each time point for a total of three samples per time point). After fixation was complete, the cells were washed in Millonig's buffer, and incubated for 2 h in 1.0% osmium tetroxide, in the same buffer. Following rinsing steps in ultrapure water and *en bloc* staining with 2.0% uranyl acetate, the samples were dehydrated in a series of graded ethanol washes and infiltrated and embedded in Spurr's plastic resin (E.M. Sciences). Embedded blocks were sectioned using a Leica UC7 Ultramicrotome, and 70- to 80-nm sections were collected on 200 mesh copper grids, and post-stained with Reynold's lead citrate. Samples were examined in an FEI Tecnai Spirit Twin transmission electron microscope, operating at 80 kV.

Co-culture of iPSC-HLCs and macrophages

On the day prior to infection, MDMs from BU1, BU2, and BU3 seeded in a T75 flask were split by incubating cells with 0.1% Trypsin-EDTA solution for 15 min at 37°C and 5% CO_2 (n = 1 flask per donor). Cells were centrifuged at 300 × g for 5 min at 4°C and resuspended in 1 mL of MDM medium. Cells were counted and 1 × 10^6 cells were seeded into six-well low-attachment plates (Corning). On the day of infection, macrophages were infected with EBOV-GFP at an MOI of 10. At 1 dpi, MDMs were incubated with 1 mL of Gentle Cell Dissociation buffer (GCD; Gibco) for 2 min at 37°C and 5%CO_2. Cells were centrifuged at 300 × g for 5 min at 4°C. GCD was removed, and cell pellets were washed three times in 1 mL of PBS. After the third wash, cells were resuspended in 1 mL of the appropriate medium and seeded in six- or 12-well tissue culture plates alone or onto D20 iPSC-HLCs at a 1:1 ratio (n = 1 per donor per time point for a total of three samples per time point).

Data and code availability

All data needed to evaluate the conclusions in the paper are present in the paper and/or the supplemental information. RNA sequencing data have been deposited to Gene Expression Omnibus (GEO: GSE184640). Pluripotent stem cell lines used in this study, along with maintenance standard operating procedures and directed differentiation protocols, are available from the CReM iPSC Repository at Boston University and Boston Medical Center and can be found at http://crem.bu.edu.

SUPPLEMENTAL INFORMATION

Supplemental information can be found online at https://doi.org/10.1016/j.stemcr.2022.08.003.

AUTHOR CONTRIBUTIONS

W.A.S. differentiated iPSC-HLCs, performed EBOV infection studies and most of the post-infection experiments, was involved in data analysis, and wrote the first draft of the manuscript. L.M.S. and S.M.R. generated primary hepatocyte cultures. C.V.M., J.V.L., and F.W. performed bioinformatics analyses. J.G.B. performed the EM analysis. S.M., R.F.J., and A.J.H. performed BSL-4 infection studies. E.L.S. performed FISH analysis, imaging, and image quantification. J.O. performed RNA and Luminex analysis. A.M. performed RNA analysis. E.Y.F. performed functional assays of the PHHs. S.N.B. was involved in the design of the primary hepatocyte experiments. E.M. and G.M. designed and directed the study, performed data analysis and interpretation, and edited the manuscript.

ACKNOWLEDGMENTS

We would like to thank H. Feldmann, J. Connor, and the World Reference Center for Emerging Viruses and Arboviruses for providing virus stocks; J. Alonso and H. Green for providing cells; and G. Olinger and the Defense Biological Product Assurance Office (DBPAO) through BEI for providing antibodies. This work was supported by NIH grants R21AI137793 (to G.M. and E.M.), N0175N92020C00005 (to G.M.), R21AI135912 (to E.M.), R01AI133486 (to E.M.), and NIH training grants T32HL007035 (to E.L.S.) and TL1TR001410 (to W.A.S.). S.N.B. is a Howard Hughes Medical Institute Investigator.

CONFLICTS OF INTEREST

The authors declare no competing interests.

Received: February 16, 2022
Revised: August 8, 2022
Accepted: August 9, 2022
Published: September 8, 2022

REFERENCES

Ben-David, U., Siranosian, B., Ha, G., Tang, H., Oren, Y., Hinohara, K., Strathdee, C.A., Dempster, J., Lyons, N.J., Burns, R., et al. (2018). Genetic and transcriptional evolution alters cancer cell line drug response. Nature *560*, 325–330. https://doi.org/10.1038/s41586-018-0409-3.

Boj, S.F., Parrizas, M., Maestro, M.A., and Ferrer, J. (2001). A transcription factor regulatory circuit in differentiated pancreatic cells. Proc. Natl. Acad. Sci. USA *98*, 14481–14486. https://doi.org/10.1073/pnas.241349398.

Busse, D.C., Habgood-Coote, D., Clare, S., Brandt, C., Bassano, I., Kaforou, M., Herberg, J., Levin, M., Eléouët, J.F., Kellam, P., and Tregoning, J.S. (2020). Interferon-induced protein 44 and interferon-induced protein 44-like restrict replication of respiratory syncytial virus. J. Virol. *94*, e00297-20. https://doi.org/10.1128/JVI.00297-20.

Caballero, I.S., Honko, A.N., Gire, S.K., Winnicki, S.M., Melé, M., Gerhardinger, C., Lin, A.E., Rinn, J.L., Sabeti, P.C., Hensley, L.E., and Connor, J.H. (2016). In vivo Ebola virus infection leads to a strong innate response in circulating immune cells. BMC Genom. *17*, 707. https://doi.org/10.1186/s12864-016-3060-0.

Carlton-Smith, C., and Elliott, R.M. (2012). Viperin, MTAP44, and protein kinase R contribute to the interferon-induced inhibition of Bunyamwera Orthobunyavirus replication. J. Virol. *86*, 11548–11557. https://doi.org/10.1128/JVI.01773-12.

Chen, A.X., Chhabra, A., Song, H.H.G., Fleming, H.E., Chen, C.S., and Bhatia, S.N. (2020). Controlled apoptosis of stromal cells to engineer human microlivers. Adv. Funct. Mater. *30*, 1910442. https://doi.org/10.1002/adfm.201910442.

de Wit, E., Rosenke, K., Fischer, R.J., Marzi, A., Prescott, J., Bushmaker, T., van Doremalen, N., Emery, S.L., Falzarano, D., Feldmann, F., et al. (2016). Ebola laboratory response at the eternal love winning africa campus, monrovia, Liberia, 2014-2015. J. Infect. Dis. *214*, S169–S176. https://doi.org/10.1093/infdis/jiw216.

Donato, M.T., Jover, R., and Gómez-Lechón, M.J. (2013). Hepatic cell lines for drug hepatotoxicity testing: limitations and strategies to upgrade their metabolic competence by gene engineering. Curr. Drug Metab. *14*, 946–968. https://doi.org/10.2174/1389200211314090002.

Feldmann, H., and Geisbert, T.W. (2011). Ebola haemorrhagic fever. Lancet *377*, 849–862. https://doi.org/10.1016/S0140-6736(10)60667-8.

Fischer, L., Lucendo-Villarin, B., Hay, D.C., and O'Farrelly, C. (2020). Human PSC-derived hepatocytes express low levels of viral pathogen recognition receptors, but are capable of mounting an effective innate immune response. Int. J. Mol. Sci. *21*, E3831. https://doi.org/10.3390/ijms21113831.

Geisbert, T.W., Hensley, L.E., Jahrling, P.B., Larsen, T., Geisbert, J.B., Paragas, J., Young, H.A., Fredeking, T.M., Rote, W.E., and Vlasuk, G.P. (2003a). Treatment of Ebola virus infection with a recombinant inhibitor of factor VIIa/tissue factor: a study in rhesus monkeys. Lancet *362*, 1953–1958. https://doi.org/10.1016/S0140-6736(03)15012-X.

Geisbert, T.W., Hensley, L.E., Larsen, T., Young, H.A., Reed, D.S., Geisbert, J.B., Scott, D.P., Kagan, E., Jahrling, P.B., and Davis, K.J. (2003b). Pathogenesis of Ebola hemorrhagic fever in cynomolgus macaques: evidence that dendritic cells are early and sustained targets of infection. Am. J. Pathol. *163*, 2347–2370. https://doi.org/10.1016/S0002-9440(10)63591-2.

Geisbert, T.W., Young, H.A., Jahrling, P.B., Davis, K.J., Kagan, E., and Hensley, L.E. (2003c). Mechanisms underlying coagulation abnormalities in ebola hemorrhagic fever: overexpression of tissue factor in primate monocytes/macrophages is a key event. J. Infect. Dis. *188*, 1618–1629. https://doi.org/10.1086/379724.

Geisbert, T.W., Young, H.A., Jahrling, P.B., Davis, K.J., Larsen, T., Kagan, E., and Hensley, L.E. (2003d). Pathogenesis of Ebola hemorrhagic fever in primate models: evidence that hemorrhage is not a direct effect of virus-induced cytolysis of endothelial cells. Am. J. Pathol. *163*, 2371–2382. https://doi.org/10.1016/S0002-9440(10)63592-4.

Greenberg, A., Huber, B.R., Liu, D.X., Logue, J.P., Hischak, A.M.W., Hart, R.J., Abbott, M., Isic, N., Hisada, Y.M., Mackman, N., et al. (2020). Quantification of viral and host biomarkers in the liver of rhesus macaques: a longitudinal study of Zaire ebolavirus strain kikwit (EBOV/Kik). Am. J. Pathol. *190*, 1449–1460. https://doi.org/10.1016/j.ajpath.2020.03.003.

Gural, N., Mancio-Silva, L., Miller, A.B., Galstian, A., Butty, V.L., Levine, S.S., Patrapuvich, R., Desai, S.P., Mikolajczak, S.A., Kappe, S.H.I., et al. (2018). In vitro culture, drug sensitivity, and transcriptome of plasmodium vivax hypnozoites. Cell Host Microbe *23*, 395–406.e4. https://doi.org/10.1016/j.chom.2018.01.002.

Hartman, A.L., Ling, L., Nichol, S.T., and Hibberd, M.L. (2008). Whole-genome expression profiling reveals that inhibition of host innate immune response pathways by Ebola virus can be reversed by a single amino acid change in the VP35 protein. J. Virol. *82*, 5348–5358. https://doi.org/10.1128/JVI.00215-08.

Hölzer, M., Krähling, V., Amman, F., Barth, E., Bernhart, S.H., Carmelo, V.A.O., Collatz, M., Doose, G., Eggenhofer, F., Ewald, J., et al. (2016). Differential transcriptional responses to Ebola and Marburg virus infection in bat and human cells. Sci. Rep. *6*, 34589. https://doi.org/10.1038/srep34589.

Hume, A.J., Heiden, B., Olejnik, J., Suder, E.L., Ross, S., Scoon, W.A., Bullitt, E., Ericsson, M., White, M.R., Turcinovic, J., et al. (2022). Recombinant Lloviu virus as a tool to study viral replication and host responses. PLoS Pathog. *18*, e1010268. https://doi.org/10.1371/journal.ppat.1010268.

Ingelman-Sundberg, M., Sim, S.C., Gomez, A., and Rodriguez-Antona, C. (2007). Influence of cytochrome P450 polymorphisms on drug therapies: pharmacogenetic, pharmacoepigenetic and clinical aspects. Pharmacol. Ther. *116*, 496–526. https://doi.org/10.1016/j.pharmthera.2007.09.004.

Jankeel, A., Menicucci, A.R., Woolsey, C., Fenton, K.A., Mendoza, N., Versteeg, K., Cross, R.W., Geisbert, T.W., and Messaoudi, I. (2020). Early transcriptional changes within liver, adrenal gland, and lymphoid tissues significantly contribute to ebola virus pathogenesis in cynomolgus macaques. J. Virol. *94*, e00250-20. https://doi.org/10.1128/JVI.00250-20.

Jasenosky, L.D., Cadena, C., Mire, C.E., Borisevich, V., Haridas, V., Ranjbar, S., Nambu, A., Bavari, S., Soloveva, V., Sadukhan, S., et al. (2019). The FDA-approved oral drug nitazoxanide amplifies host antiviral responses and inhibits ebola virus. iScience *19*, 1279–1290. https://doi.org/10.1016/j.isci.2019.07.003.

Kash, J.C., Mühlberger, E., Carter, V., Grosch, M., Perwitasari, O., Proll, S.C., Thomas, M.J., Weber, F., Klenk, H.D., and Katze, M.G. (2006). Global suppression of the host antiviral response by Ebola- and Marburgviruses: increased antagonism of the type I interferon response is associated with enhanced virulence. J. Virol. *80*, 3009–3020. https://doi.org/10.1128/JVI.80.6.3009-3020.2006.

Khetani, S.R., and Bhatia, S.N. (2008). Microscale culture of human liver cells for drug development. Nat. Biotechnol. *26*, 120–126. https://doi.org/10.1038/nbt1361.

Kolesnikova, L., Nanbo, A., Becker, S., and Kawaoka, Y. (2017). Inside the cell: assembly of filoviruses. Curr. Top. Microbiol. Immunol. *411*, 353–380. https://doi.org/10.1007/82_2017_15.

Kotliar, D., Lin, A.E., Logue, J., Hughes, T.K., Khoury, N.M., Raju, S.S., Wadsworth, M.H., 2nd, Chen, H., Kurtz, J.R., Dighero-Kemp, B., et al. (2020). Single-cell profiling of ebola virus disease in vivo reveals viral and host dynamics. Cell *183*, 1383–1401.e19. https://doi.org/10.1016/j.cell.2020.10.002.

Kuzmin, I.V., Schwarz, T.M., Ilinykh, P.A., Jordan, I., Ksiazek, T.G., Sachidanandam, R., Basler, C.F., and Bukreyev, A. (2017). Innate immune responses of bat and human cells to filoviruses: commonalities and distinctions. J. Virol. *91*, e02471-16. https://doi.org/10.1128/JVI.02471-16.

Kwiterovich, P.O., Jr. (2000). The metabolic pathways of high-density lipoprotein, low-density lipoprotein, and triglycerides: a current review. Am. J. Cardiol. *86*, 5L–10L. https://doi.org/10.1016/s0002-9149(00)01461-2.

Lang, J., Vera, D., Cheng, Y., and Tang, H. (2016). Modeling dengue virus-hepatic cell interactions using human pluripotent stem cell-derived hepatocyte-like cells. Stem Cell Rep. *7*, 341–354. https://doi.org/10.1016/j.stemcr.2016.07.012.

Lanini, S., Portella, G., Vairo, F., Kobinger, G.P., Pesenti, A., Langer, M., Kabia, S., Brogiato, G., Amone, J., Castilletti, C., et al. (2018). Relationship between viremia and specific organ damage in ebola patients: a cohort study. Clin. Infect. Dis. *66*, 36–44. https://doi.org/10.1093/cid/cix704.

Li, K., Chen, Z., Kato, N., Gale, M., Jr., and Lemon, S.M. (2005). Distinct poly(I-C) and virus-activated signaling pathways leading to interferon-beta production in hepatocytes. J. Biol. Chem. *280*, 16739–16747. https://doi.org/10.1074/jbc.M414139200.

Liao, Y., Wang, J., Jaehnig, E.J., Shi, Z., and Zhang, B. (2019). WebGestalt 2019: gene set analysis toolkit with revamped UIs and APIs. Nucleic Acids Res. *47*, W199–W205. https://doi.org/10.1093/nar/gkz401.

Liu, X., Speranza, E., Muñoz-Fontela, C., Haldenby, S., Rickett, N.Y., Garcia-Dorival, I., Fang, Y., Hall, Y., Zekeng, E.G., Lüdtke, A., et al. (2017). Transcriptomic signatures differentiate survival from fatal outcomes in humans infected with Ebola virus. Genome Biol. *18*, 4. https://doi.org/10.1186/s13059-016-1137-3.

March, S., Ramanan, V., Trehan, K., Ng, S., Galstian, A., Gural, N., Scull, M.A., Shlomai, A., Mota, M.M., Fleming, H.E., et al. (2015). Micropatterned coculture of primary human hepatocytes and supportive cells for the study of hepatotropic pathogens. Nat. Protoc. *10*, 2027–2053. https://doi.org/10.1038/nprot.2015.128.

Marozin, S., Altomonte, J., Stadler, F., Thasler, W.E., Schmid, R.M., and Ebert, O. (2008). Inhibition of the IFN-beta response in hepatocellular carcinoma by alternative spliced isoform of IFN regulatory factor-3. Mol. Ther. *16*, 1789–1797. https://doi.org/10.1038/mt.2008.201.

Martines, R.B., Ng, D.L., Greer, P.W., Rollin, P.E., and Zaki, S.R. (2015). Tissue and cellular tropism, pathology and pathogenesis of Ebola and Marburg viruses. J. Pathol. *235*, 153–174. https://doi.org/10.1002/path.4456.

McElroy, A.K., Harmon, J.R., Flietstra, T.D., Campbell, S., Mehta, A.K., Kraft, C.S., Lyon, M.G., Varkey, J.B., Ribner, B.S., Kratochvil, C.J., et al. (2016). Kinetic analysis of biomarkers in a cohort of US patients with ebola virus disease. Clin. Infect. Dis. *63*, 460–467. https://doi.org/10.1093/cid/ciw334.

McElroy, A.K., Mühlberger, E., and Muñoz-Fontela, C. (2018). Immune barriers of Ebola virus infection. Curr. Opin. Virol. *28*, 152–160. https://doi.org/10.1016/j.coviro.2018.01.010.

Michailidis, E., Vercauteren, K., Mancio-Silva, L., Andrus, L., Jahan, C., Ricardo-Lax, I., Zou, C., Kabbani, M., Park, P., Quirk, C., et al. (2020). Expansion, in vivo-ex vivo cycling, and genetic manipulation of primary human hepatocytes. Proc. Natl. Acad. Sci. USA *117*, 1678–1688. https://doi.org/10.1073/pnas.1919035117.

Olejnik, J., Forero, A., Deflubé, L.R., Hume, A.J., Manhart, W.A., Nishida, A., Marzi, A., Katze, M.G., Ebihara, H., Rasmussen, A.L., and Mühlberger, E. (2017). Ebolaviruses associated with differential pathogenicity induce distinct host responses in human macrophages. J. Virol. *91*, e00179-17. https://doi.org/10.1128/JVI.00179-17.

Park, S., Gianotti-Sommer, A., Molina-Estevez, F.J., Vanuytsel, K., Skvir, N., Leung, A., Rozelle, S.S., Shaikho, E.M., Weir, I., Jiang, Z., et al. (2017). A comprehensive, ethnically diverse library of sickle cell disease-specific induced pluripotent stem cells. Stem Cell Rep. *8*, 1076–1085. https://doi.org/10.1016/j.stemcr.2016.12.017.

Power, D., Santoso, N., Dieringer, M., Yu, J., Huang, H., Simpson, S., Seth, I., Miao, H., and Zhu, J. (2015). IFI44 suppresses HIV-1 LTR promoter activity and facilitates its latency. Virology *481*, 142–150. https://doi.org/10.1016/j.virol.2015.02.046.

Rollin, P.E., Bausch, D.G., and Sanchez, A. (2007). Blood chemistry measurements and D-Dimer levels associated with fatal and nonfatal outcomes in humans infected with Sudan Ebola virus. J. Infect. Dis. *196*, S364–S371.

Sakurai, F., Mitani, S., Yamamoto, T., Takayama, K., Tachibana, M., Watashi, K., Wakita, T., Iijima, S., Tanaka, Y., and Mizuguchi, H. (2017). Human induced-pluripotent stem cell-derived hepatocyte-like cells as an in vitro model of human hepatitis B virus infection. Sci. Rep. *7*, 45698. https://doi.org/10.1038/srep45698.

Schwartz, R.E., Trehan, K., Andrus, L., Sheahan, T.P., Ploss, A., Duncan, S.A., Rice, C.M., and Bhatia, S.N. (2012). Modeling hepatitis C virus infection using human induced pluripotent stem cells. Proc. Natl. Acad. Sci. USA *109*, 2544–2548. https://doi.org/10.1073/pnas.1121400109.

Shlomai, A., Schwartz, R.E., Ramanan, V., Bhatta, A., de Jong, Y.P., Bhatia, S.N., and Rice, C.M. (2014). Modeling host interactions with hepatitis B virus using primary and induced pluripotent stem cell-derived hepatocellular systems. Proc. Natl. Acad. Sci. USA *111*, 12193–12198. https://doi.org/10.1073/pnas.1412631111.

Smither, S.J., O'Brien, L.M., Eastaugh, L., Woolley, T., Lever, S., Fletcher, T., Parmar, K., Hunt, B.J., Watts, S., and Kirkman, E. (2019). Haemostatic changes in five patients infected with ebola virus. Viruses *11*. https://doi.org/10.3390/v11070647.

Somers, A., Jean, J.C., Sommer, C.A., Omari, A., Ford, C.C., Mills, J.A., Ying, L., Sommer, A.G., Jean, J.M., Smith, B.W., et al. (2010). Generation of transgene-free lung disease-specific human induced pluripotent stem cells using a single excisable lentiviral stem cell cassette. Stem Cell. *28*, 1728–1740. https://doi.org/10.1002/stem.495.

Towner, J.S., Paragas, J., Dover, J.E., Gupta, M., Goldsmith, C.S., Huggins, J.W., and Nichol, S.T. (2005). Generation of eGFP expressing recombinant Zaire ebolavirus for analysis of early pathogenesis events and high-throughput antiviral drug screening. Virology *332*, 20–27.

Tricot, T., Helsen, N., Kaptein, S.J.F., Neyts, J., and Verfaillie, C.M. (2018). Human stem cell-derived hepatocyte-like cells support Zika virus replication and provide a relevant model to assess the efficacy of potential antivirals. PLoS One *13*, e0209097. https://doi.org/10.1371/journal.pone.0209097.

Uyeki, T.M., Mehta, A.K., Davey, R.T., Jr., Liddell, A.M., Wolf, T., Vetter, P., Schmiedel, S., Grünewald, T., Jacobs, M., Arribas, J.R., et al. (2016). Clinical management of ebola virus disease in the United States and europe. N. Engl. J. Med. *374*, 636–646. https://doi.org/10.1056/NEJMoa1504874.

Ward, M.D., Brueggemann, E.E., Kenny, T., Reitstetter, R.E., Mahone, C.R., Trevino, S., Wetzel, K., Donnelly, G.C., Retterer, C., Norgren, R.B., Jr., et al. (2019). Characterization of the plasma proteome of nonhuman primates during Ebola virus disease or melioidosis: a host response comparison. Clin. Proteomics *16*, 7. https://doi.org/10.1186/s12014-019-9227-3.

Wilson, A.A., Ying, L., Liesa, M., Segeritz, C.P., Mills, J.A., Shen, S.S., Jean, J., Lonza, G.C., Liberti, D.C., Lang, A.H., et al. (2015). Emergence of a stage-dependent human liver disease signature with directed differentiation of alpha-1 antitrypsin-deficient iPS cells. Stem Cell Rep. *4*, 873–885. https://doi.org/10.1016/j.stemcr.2015.02.021.

Xiang, C., Du, Y., Meng, G., Soon Yi, L., Sun, S., Song, N., Zhang, X., Xiao, Y., Wang, J., Yi, Z., et al. (2019). Long-term functional maintenance of primary human hepatocytes in vitro. Science *364*, 399–402. https://doi.org/10.1126/science.aau7307.

Zaki, S.R., and Goldsmith, C.S. (1999). Pathologic features of filovirus infections in humans. Curr. Top. Microbiol. Immunol. *235*, 97–116.

Zhou, X., Sun, P., Lucendo-Villarin, B., Angus, A.G.N., Szkolnicka, D., Cameron, K., Farnworth, S.L., Patel, A.H., and Hay, D.C. (2014). Modulating innate immunity improves hepatitis C virus infection and replication in stem cell-derived hepatocytes. Stem Cell Rep. *3*, 204–214. https://doi.org/10.1016/j.stemcr.2014.04.018.

Stem Cell Reports, Volume *17*

Supplemental Information

Ebola virus infection induces a delayed type I IFN response in bystander cells and the shutdown of key liver genes in human iPSC-derived hepatocytes

Whitney A. Scoon, Liliana Mancio-Silva, Ellen L. Suder, Carlos Villacorta-Martin, Jonathan Lindstrom-Vautrin, John G. Bernbaum, Steve Mazur, Reed F. Johnson, Judith Olejnik, Elizabeth Y. Flores, Aditya Mithal, Feiya Wang, Adam J. Hume, Joseph E. Kaserman, Sandra March-Riera, Andrew A. Wilson, Sangeeta N. Bhatia, Elke Mühlberger, and Gustavo Mostoslavsky

Supplemental information

Supplemental Methods

Vesicular Stomatitis Virus

Recombinant vesicular stomatitis virus (VSV) expressing GFP or mCherry from an additional transcription unit (VSV-GFP and VSV-mCherry; kindly provided by J. Connor, Boston University) was propagated in Vero E6. Viral titers were determined by $TCID_{50.}$

qRT-PCR Analysis

Cells were harvested for RNA analysis by using either the RNeasy Kit (Qiagen) or TRIzol Reagent (ThermoFisher) according to manufacturer's instructions. For hepatic cellular markers, the TaqMan qRT-PCR system (ThermoFisher) was used. cDNA libraries of the harvested cellular RNA were prepared using SuperScript III Reverse Transcriptase (ThermoFisher). 500 ng of the cDNA library was added to a TaqMan probe reaction master mix containing 10 μL of the TaqMan Universal PCR Master Mix 2x Buffer, 1 μL of TaqMan gene probe, and nuclease-free water to a final volume of 20 μL per reaction. For qRT-PCR of IFNβ, $1x10^6$ or $4x10^5$ iPSC-HLCs and Huh7 cells were harvested 1 day post-VSV infection by using TRIzol Reagent (ThermoFisher) according to manufacturer's instructions. The QuantiTect SYBR Green RT-PCR kit was used (Qiagen) for qRT-PCR analysis. 50 ng of purified cellular RNA was added to a SYBR Green reaction master mix containing 12.5 μL of SYBR master mix, 2.5 μL of QuantiTect gene probe, 0.25 μL of QuantiTect Reverse Transcriptase mix, and nuclease-free water to a final volume of 25 μL per reaction. For both systems, triplicate samples (n= 3 per gene per sample) were run on a StepOnePlus Real Time PCR machine (ThermoFisher). CT values were plotted using Prism GraphPad Software. Statistical significance was determined by paired t-tests with comparisons of interest plotted on each graph.

Immunofluorescence Analysis

$1x10^6$ or $4x10^5$ cells were fixed with either 4% PFA in DMEM for 10 minutes at room temperature or 10% formalin for at least 6 hours at 4°C. Cells were washed in PBS, permeabilized with a solution of acetone-methanol in a 1:1 volume ratio for 5 minutes at -20°C and incubated in blocking buffer for at least 20 minutes at room temperature. Due to cross-reactivity with the BSA in the blocking buffer, the cells were not incubated in blocking buffer when stained for albumin. Cells were incubated with primary antibody overnight at 4°C, and primary antibody names and dilutions are listed in Table S3. Cells were incubated with secondary antibody and 4′,6-diamidino-2-phenylindole (DAPI) for one hour at room temperature (dilutions listed in Table S3).

Illumina Sequencing

Duplicate samples of $1x10^6$ BU3 iPSC-HLCs were mock-infected or infected with EBOV at an MOI of 10 (n = 2 per condition per time point). Cells were harvested for RNA analysis at 1, 2, 3, and 7 dpi using TRIzol reagent (ThermoFisher). RNA was isolated according to manufacturer's instructions. 1 µg of purified cellular RNA was diluted to a concentration of 50 ng/µL in a final volume of 20 µL and shipped to Novogene on dry ice for library preparation and Illumina sequencing. The quality of the raw data was assessed using FastQC v.0.11.7. The sequence reads were aligned to a combination of the human genome reference (GRCh38) and the EBOV reference sequence (NC_002549.1) using STAR v.2.6.0c. Counts per gene were summarized using the featureCounts function from the subread package v.1.6.2. Log counts per million (lcpm) per gene were averaged across both technical duplicates for each sample. After exploratory data analysis (Glimma v. 1.11.1), contrasts for differential expression testing were done for each EBOV-infected sample compared to the mock control at each time point separately. Statistical significance of the logFC for each time point contrast was determined by a paired t-test and reported as a Benjamini-Hochberg false discovery rate adjusted p-value. Gene Set Enrichment Analysis (GSEA) was performed using all genes in the dataset, ranked on logFC, using WebGestalt to analyze Biological Processes in GO databases or the Reactome in Pathway databases with the following parameters: minimum number of genes in a category = 15; false discovery rate (FDR) ≤ 0.01; permutations = 1000 (Liao et al., 2019). All RNA-Seq data have been deposited to Gene Expression Omnibus (GEO id GSE184640).

Fluorescence in-situ Hybridization Assay

Fluorescence in-situ hybridization (RNA-FISH) was performed using the Advanced Cell Diagnostics RNAscope v2 kit according to manufacturer's instructions (ACD Bio). 5x10^5 BU1, BU2, and BU3 iPSC-HLCs were seeded onto 2 well glass chamber slides, and 1x10^5 Huh7 cells were seeded onto 8 well glass chamber slides. Replicates per experiment varied by condition and are listed in the corresponding figure legends. Both cell types were infected at an MOI of 10 as described above. Cells were fixed with 10% formalin for a minimum of 6 hours. After fixation, cells were dehydrated with ethanol washes before being stored in 100% ethanol at -20ºC until staining. On the day of the assay, cells were rehydrated with ethanol. Cells were pre-treated with hydrogen peroxidase and Protease III according to the manufacturer's instructions. Cells were probed with RNAscope probes for 2 hours at 40ºC in the ACD hybridization oven. The following probes (all from ACD Bio) were used: ebolavirus Zaire VP35- C1 (undiluted), human IL6- C2 (1:50), human IFNβ- C3 (1:50), human CXCL10- C3 (1:50). After hybridization, the cells were treated with the amplification and development reagents according to manufacturer's instructions. An additional blocking and washing step was added following amplification of channels containing viral RNA probes to prevent cross-reaction due to viral gene abundance. Fluorophores used for detection (Perkin Elmer) include Opal 520 (1:3000), Opal 570 (1:3000), and Opal 690 (1:1500). Samples were visualized on a Nikon Eclipse Ti2 inverted microscope using Photometrics Prime BSI camera, and quantification of gene-expressing cells was performed in QuPath software (https://doi.org/10.1038/S41598-017-17204-50) using the cell detection feature and manual identification of positive cells.

Immortalized Cell Culture

Vero E6 (Cercopithecus aethiops kidney cell line, ATCC CRL-1586) and Huh-7 cells (human hepatocellular carcinoma cell line, kindly provided by J. Alonso, Texas Biomedical Research Institute, San Antonio, TX) were maintained in Dulbecco's Modified Eagle Media (DMEM) (Gibco), 10% fetal bovine serum (FBS), 200 nM L-glutamine in solution, and 5000 units/mL Penicillin Streptomycin solution. Cells were incubated at 37°C with 5% CO_2.

Flow Cytometry Analysis

$2.5x10^5$ D0 and D5 BU2 cells (n = 5) were stained for flow cytometry analysis of the endoderm markers cKit and CXCR4. Cells were harvested by centrifugation at 300xg at 4°C for 5 minutes. Cells were resuspended in PBS and stained with APC-conjugated cKit (BioLegend) and PE-conjugated CXCR4 (Invitrogen) primary antibodies for 30 minutes. Cells were washed with FACS buffer and filtered through a 35 µm filter into a 5 mL polystyrene FACS tube and analyzed on a Stratadigm Flow Cytometry machine or a FACS Calibur Flow Cytometry machine. Analysis of the flow plots was performed using FlowJo.

Periodic Acid-Schiff (PAS) Staining

PAS staining was performed on triplicate samples of $1x10^6$ BU2 iPSC-HLCs, $1x10^6$ Huh7 cells, and $1x10^4$ Donor A PHHs using the Periodic Acid-Schiff (PAS) kit (Sigma-Aldrich) according to manufacturer's instructions (n = 3 for each cell type). Cells were fixed with 1 mL of 4% paraformaldehyde (PFA) solution for 10 minutes at room temperature prior to PAS staining. PBS was added to the cells for imaging on an inverted microscope.

LDL-Uptake Assay

Duplicate samples of $1x10^6$ BU1 and BU2 iPSC-HLCs, $1x10^6$ Huh7 cells, and $1x10^4$ PHHs were analyzed using the LDL Uptake Assay Kit (Cell-Based) (Abcam) according to manufacturer's instructions (n = 2 for each donor and cell type). The LDL-DyLight reagent was diluted in the appropriate cell culture medium for each cell type. The cells were incubated with the LDL reagents at 37°C for 4 hours. Cells were washed one time with 1 mL of PBS, and 2 mL of PBS was added to the cells for visualization of LDL update on an inverted microscope with a filter capable of capturing excitation and emission wavelengths of 540 and 570 nm.

CYP3A4 P450-Glo Assay

The quantification of CYP3A4 in triplicate samples of 1x10^6 BU2 iPSCs, BU2 iPSC-HLCs, and Huh7 cells was performed using the P450-Glo Assay kit (Promega) according to manufacturer's instructions (n = 3 for each cell type). One day prior to the assay, Huh7 cells were treated with cell culture media containing 100 nM Dexamethasone. One the day of the assay, the Luciferin Glo substrate was added to the appropriate cell culture medium for each cell type. Cells were incubated with luciferin reagents at 37°C for 4 hours. Supernatant was clarified at 300xg for 5 minutes at room temperature. Clarified supernatant and detection reagent were incubated at room temperature for 20 minutes. Luminescence was measured on a LUMIStar Omega Luminometer (BMG Labtech).

VSV Bioassay

Duplicate samples of 4x10^5 iPSC-HLCs from BU1, BU2, and BU3 and triplicate samples of Huh7 cells were infected with VSV-GFP or VSV-mCherry at an MOI of 10 (n = 2 for each iPSC-HLC donor and n = 3 for Huh7 cell samples). 1 dpi, cells were imaged for GFP expression and cellular RNA was purified for qRT-PCR analysis.

Luminex analysis

Triplicate samples of 2x10^5 BU3 iPSC-HLCs cells were infected with EBOV at an MOI of 10 or left uninfected (n = 3 per condition). Cell supernatants (1mL per sample) were collected at the indicated time points. Samples were clarified by low-speed centrifugation and analyzed using the ProcartaPlex Human IP-

10 Simplex assay (Invitrogen). Mean fluorescence intensity was measured to calculate final concentration in picograms per milliliter using Bioplex200 and Bioplex Manager 5 software (Bio-Rad). Experiment was performed in triplicate. Statistical analysis of data was performed using unpaired t-test in GraphPad Prism.

SmartSeq2 Sequencing

$1x10^6$ BU1, BU2, and BU3 iPSC-HLCs or triplicate samples of Huh7 cells were seeded in 6-well tissue culture plates, and $1x10^4$ PHHs from Donor A and Donor B were seeded in 96-well glass-bottom plates (n = 1 per iPSC-HLC donor; n = 3 Huh7 cell samples; n = 2 per donor of PHHs). The cells were infected with EBOV at an MOI of 10 or left uninfected and lysed 1 dpi. Cellular RNA was isolated using TRIzol reagent (ThermoFisher) according to the manufacturer's instructions. 50 ng of purified RNA was used for sequencing by diluting to a final concentration of 5 ng/μL in a final volume of 10 μL. Samples were pipetted into a twin.tec® PCR 96-well plate (Eppendorf) and sent out for sequencing on dry ice. Sequencing was performed at the Broad Institute Genomics Services Core. The quality of the raw data was assessed using FastQC v.0.11.7. The sequence reads were aligned to a combination of the human genome reference (GRCh38) and the Ebola virus reference (NC_002549.1) using STAR v.2.6.0c. Counts per gene were summarized using the featureCounts function from the subread package v.1.6.2. The matrix of counts per gene per sample was then analyzed using the limma/voom normalization (limma v. 3.39.19, edgeR v.3.25.10). After exploratory data analysis (Glimma v. 1.11.1), contrasts for differential expression testing were done for each EBOV-infected sample compared to mock-infected samples (controls) at each time point separately. Functional predictions were performed using WebGestalt for gene set analysis (Liao *et al.*, 2019).

Luminescent Caspase 3 Assay

To quantify the activity of caspase 3 in Huh7 cells and HLCs, we utilized the Promega Caspase-Glo 3/7 Kit (cat# G8090). Triplicate samples of $1x10^5$ Huh7 cells or $4x10^5$ HLCs from bBU1, BU2, and BU3 were infected with EBOV MOI 10 or mock-infected. Cells were also treated with 2 µM Staurosporine (Sigma-Aldrich). At the designated time point, cell supernatant was mixed at a 2:1 ratio with the detection reagent from the Promega kit and incubated for 30 minutes at room temperature. 200 µL of this supernatant mixture was analyzed on a LUMIStar Omega Luminometer (BMG Labtech). Luminescent values were normalized to a blank control and reported as the fold change in luminescent activity over Mock-infected controls. Results from bBU1, BU2, and BU3 samples are averaged and represented as a single HLC sample.

Macrophage Differentiation from Peripheral Mononuclear Blood Cells

MDMs were generated from apheresed peripheral blood mononuclear cells using Ficoll separation (GE Healthcare) from BU1, BU2, and BU3 donors. Whole blood was diluted to a final volume of 30 mL with PBS. 15 mL of Ficoll was added to a 50 mL conical tube, and the diluted whole blood was overlayed onto the Ficoll. Blood was centrifuged for 30 minutes at 450xg with the brake turned off of the centrifuge. The blood separated into three layers: the off-white plasma layer, a thin white buffy coat containing leukocytes, and the pelleted erythrocytes. The plasma layer was removed, and the buffy coat was isolated into a fresh 50 mL conical tube. The buffy coat was diluted to a final volume of 50 mL using 37ºC PBS. Cells were centrifuged at 350xg for 10 minutes with the centrifuge brake on. The cell pellet was then washed three times with 50 mL of warm PBS and centrifuged at 350xg for 10 minutes. After the final wash, cells were resuspended in 1 mL of warm PBS and counted. 1×10^7 cells were plated in a T75 flask with RPMI medium for one hour at 37ºC and 5% CO_2, non-adhered cells were removed, and 10 ml RPMI medium with 10% FBS, 1% L-glutamine, 10 mM HEPES, 10ng/mL GM-CSF, and 50 U/mL penicillin with 50 mg/mL streptomycin (MDM medium) was added to the cells. Medium was changed every 2 to 3 days for a minimum of 6 days before differentiated macrophages were split into 6-well TC plates for infection experiments.

Supplementary Figures

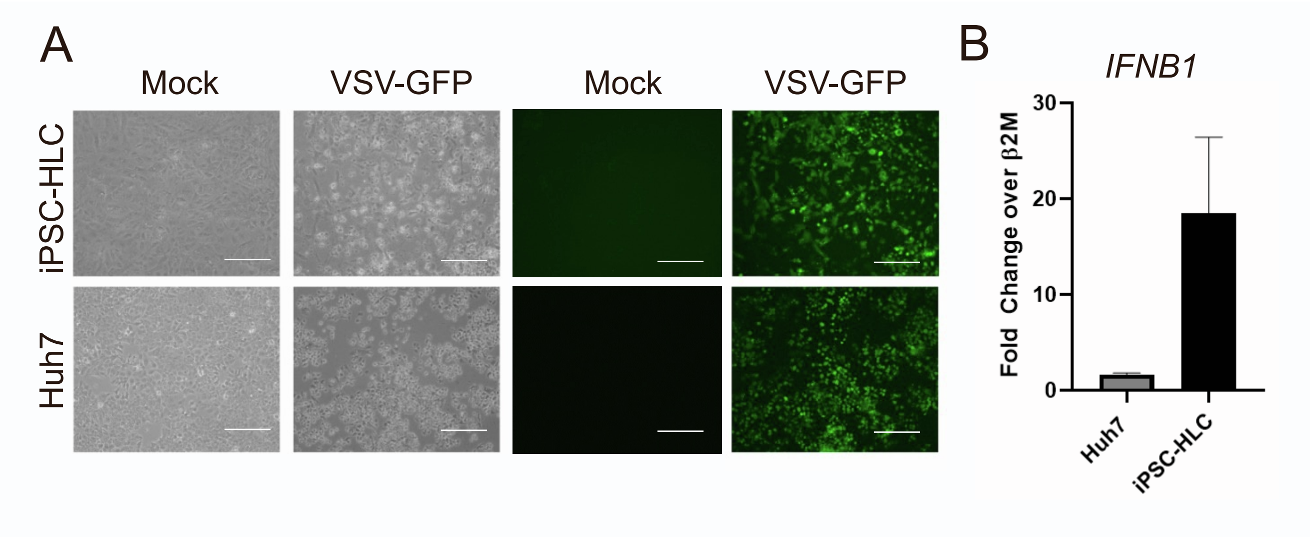

Figure S1. Induction of a type I IFN response in VSV-GFP-infected iPSC-HLCs. (A) Representative brightfield and fluorescence images of iPSC-HLCs and Huh7 cells either mock-infected or infected with VSV-GFP at an MOI of 10 at 1 dpi. Images taken at 10x magnification. Images are representative of iPSC-HLCs from three donors and three replicates of Huh7 cells. Scale bars are 20µm. (B) SYBR green qRT-PCR analysis of iPSC-HLCs and Huh7 cells infected with VSV-GFP. Expression of *IFNB1* was normalized to expression of β-2 microglobulin. Error bars represent SEM of three independent replicates of iPSC-HLCs (BU1, BU2, BU3) and three replicates of Huh7 cells.

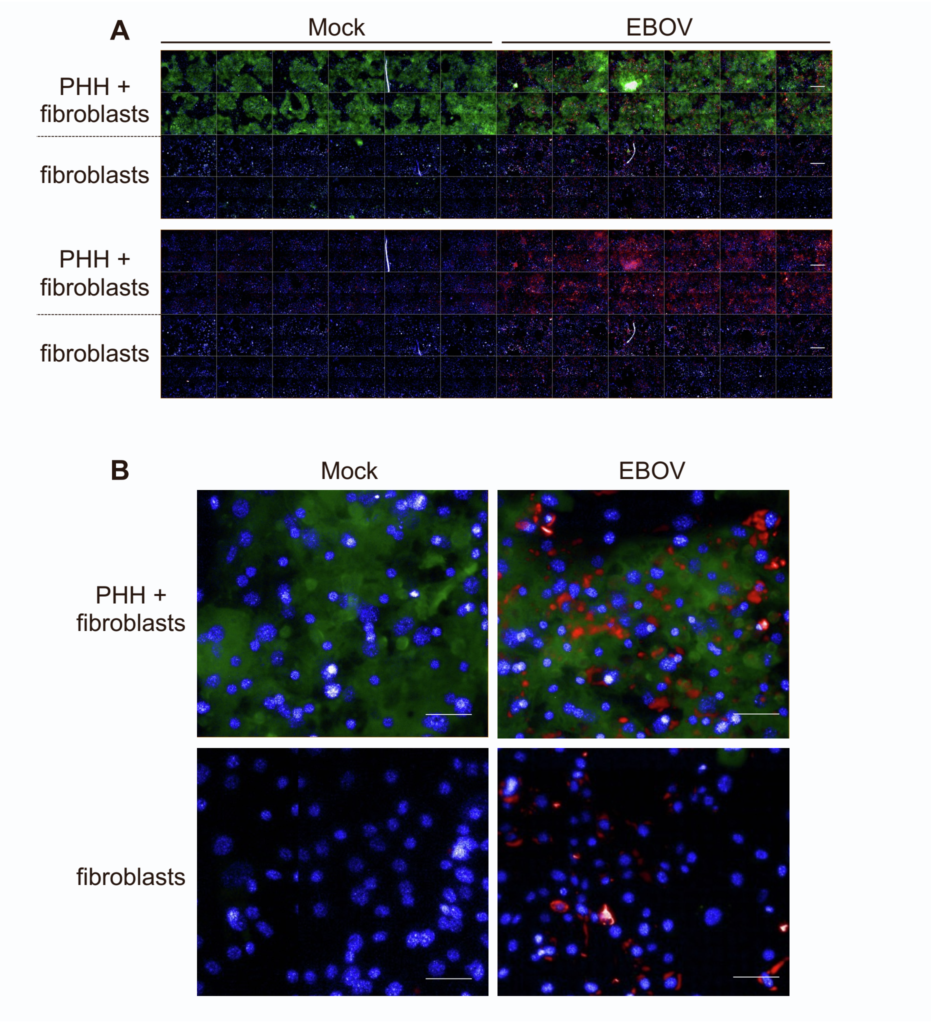

Figure S2. EBOV infection of micropatterned cocultures consisting of primary human hepatocyte islands supported by J2-3T3 murine embryonic fibroblasts. Murine fibroblasts were seeded in 96-well plates with and without primary human hepatocytes (PHH). Cells were mock-infected or infected with EBOV at an MOI of 3 and fixed at 4 dpi. Cells were immunostained with antibodies directed against the EBOV nucleoprotein (red) and human CK18 (liver cell specific; green). Cell nuclei were stained with DAPI (blue). Images captured on an Operetta at 10x magnification. (A) Representative images for donor B. Shown are images taken from three wells per condition with 4 images per well. Upper panel shows DAPI, NP, and CK18 staining, lower panel shows DAPI and NP staining only. Scale bars are 5μm. (B) Higher magnifications of the infected cells. Experiments were performed with PHHs from two donors with similar outcome. Scale bars are 20μm.

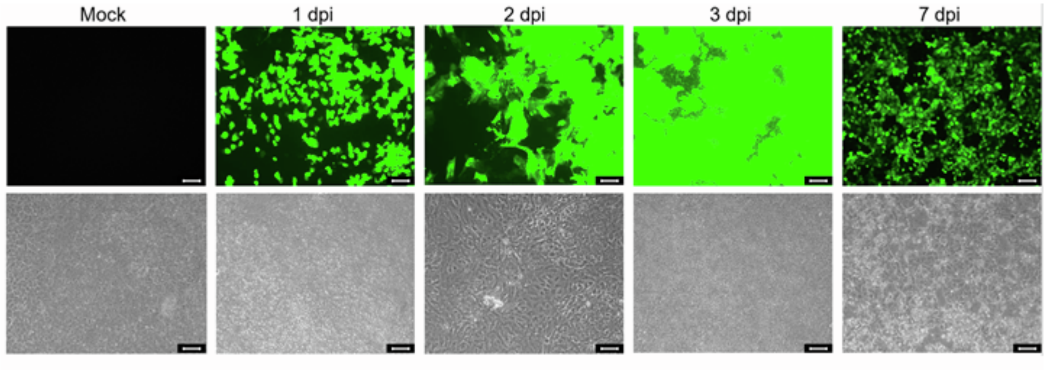

Figure S3. EBOV-infected iPSC-HLCs show CPE at late time points post infection. iPSC-HLCs were infected with EBOV-GFP at an MOI of 10 and imaged at the indicated time points. Mock-infected cells imaged at 1 dpi. Representative images from three independent experiments with similar outcome using cells from three donors (BU1-3). Scale bars are 20 µm.

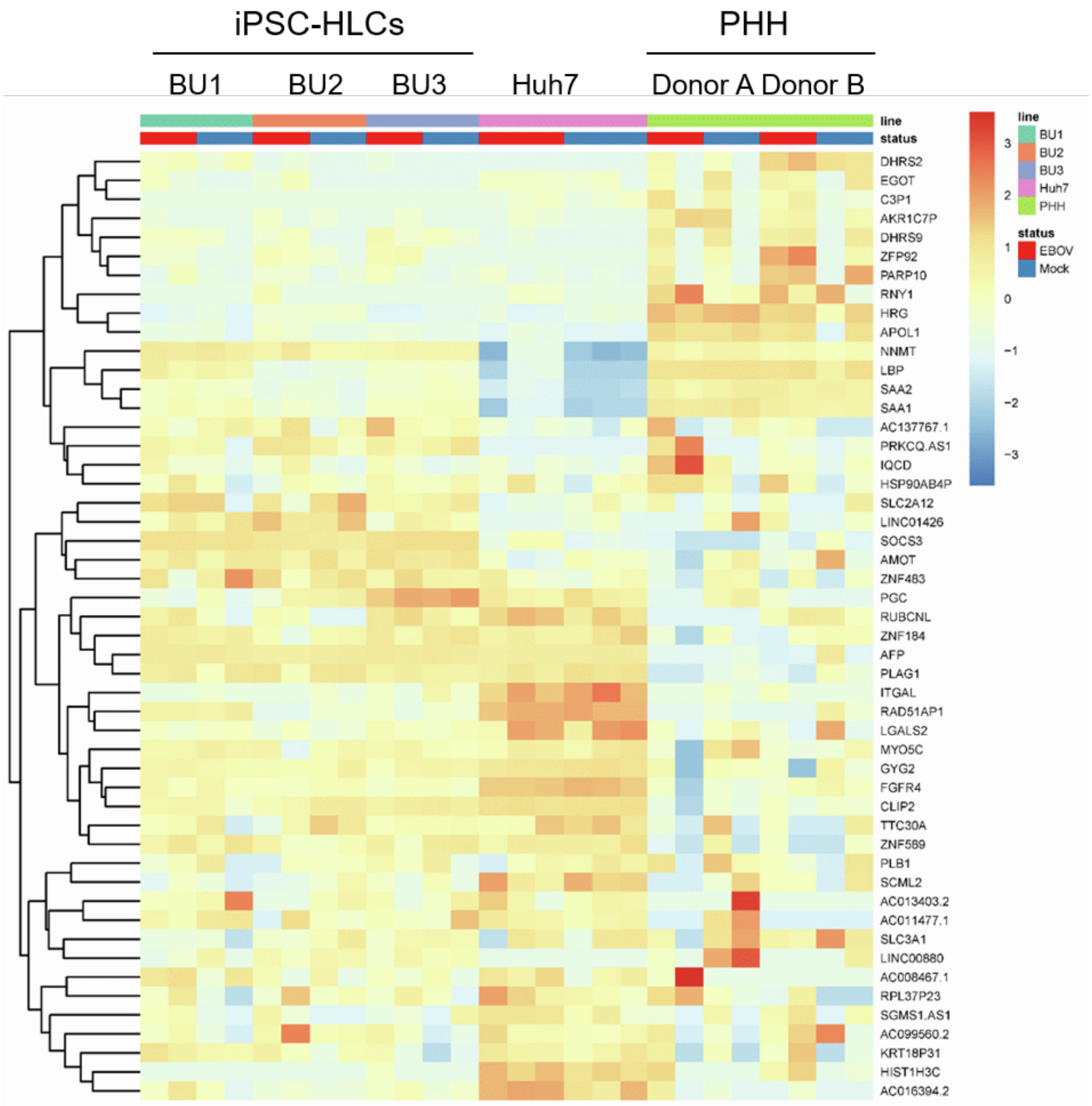

Figure S4. Hepatocytes do not respond to EBOV infection 1 dpi. Heatmap displaying the normalized relative expression of the top 50 genes ranked on absolute logFC across all EBOV-infected hepatocyte infection platforms compared to uninfected controls. No gene in this list was differentially expressed at significant levels when compared to uninfected controls (p-value ≥ 0.05). Each transcript is labeled on the right of the plot. The cell platform and infection status are color-coded on the top of the plot, and the key is located to the right of the plot. Red, EBOV; blue, Mock.

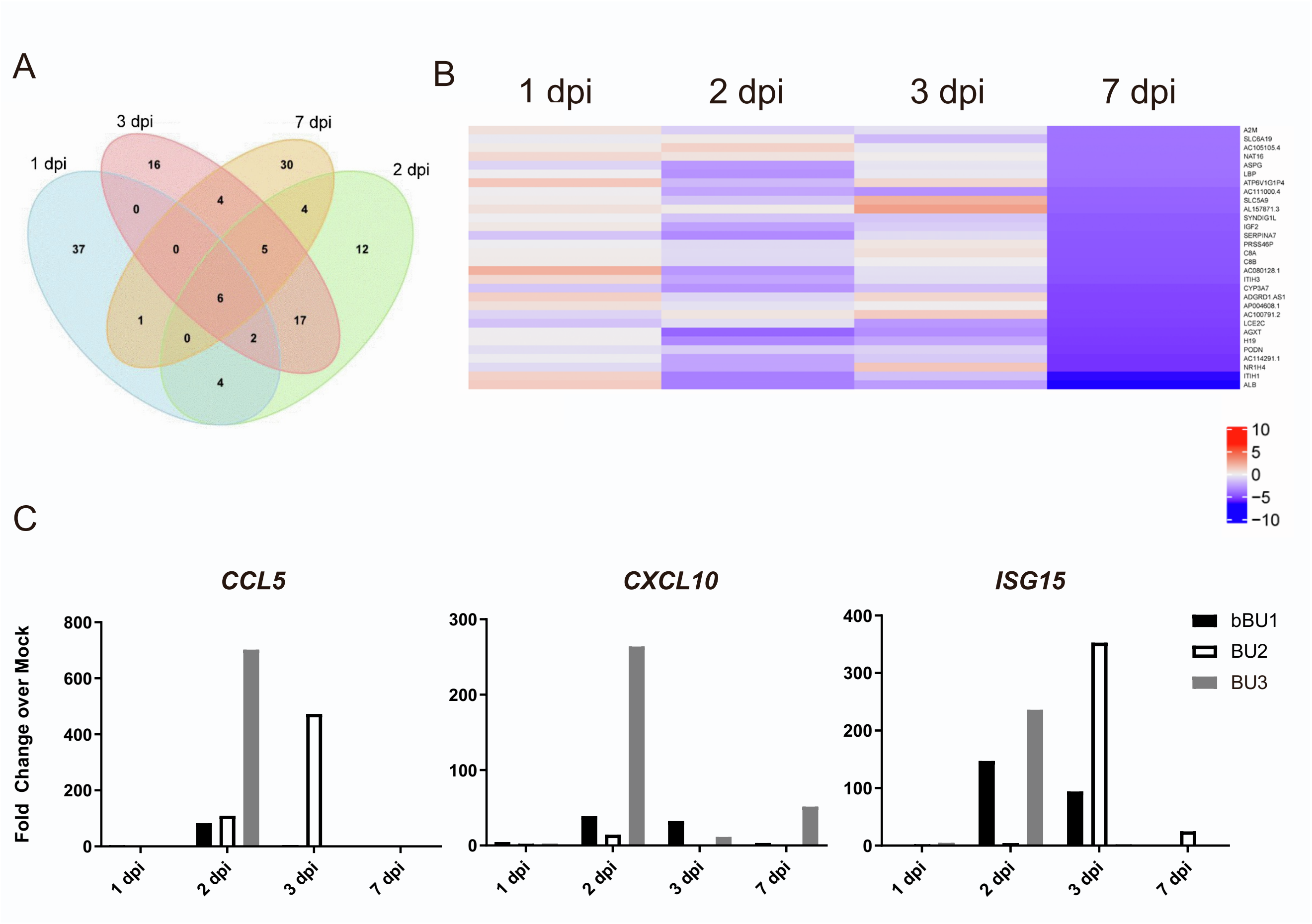

Figure S5. iPSC-HLCs respond to EBOV infection 2-7 dpi. (A) Venn diagram displaying the 50 most DEG for each time point comparison (1 dpi, 2 dpi, 3 dpi, and 7 dpi) and the number of overlapping genes between time points. (B) Heatmap displaying the logFC for the top 30 downregulated DEG at 7 dpi plotted for each time point. List of genes on the right of the heatmap. Key for the value of the logFC to the bottom left of the plot. Time point contrast labeled on the bottom of the plot. (C) qRT-PCR analysis of *CCL5*, *CXCL10* and *ISG15* in three independent iPSC-derived HLC (bBU1, BU2 and BU3) infected with EBOV at 1 dpi, 2 dpi, 3 dpi and 7 dpi.

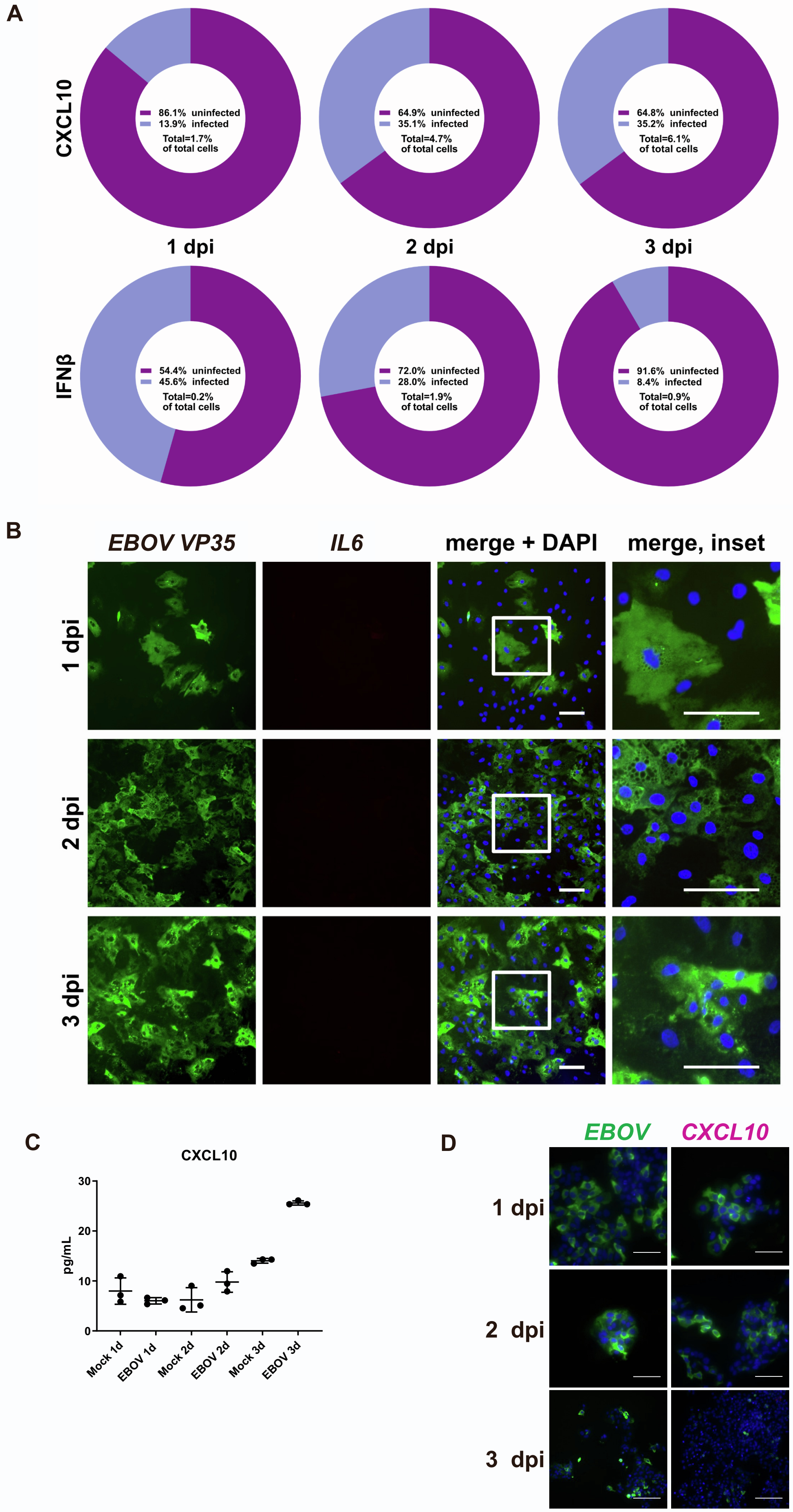
A
CXCL10
86.1% uninfected
13.9% infected
Total=1.7% of total cells
64.9% uninfected
35.1% infected
Total=4.7% of total cells
64.8% uninfected
35.2% infected
Total=6.1% of total cells
1 dpi
2 dpi
3 dpi
IFNβ
54.4% uninfected
45.6% infected
Total=0.2% of total cells
72.0% uninfected
28.0% infected
Total=1.9% of total cells
91.6% uninfected
8.4% infected
Total=0.9% of total cells
B
EBOV VP35
IL6
merge + DAPI
merge, inset
1 dpi
2 dpi
3 dpi
C
CXCL10
pg/mL
30
20
10
0
Mock 1d
EBOV 1d
Mock 2d
EBOV 2d
Mock 3d
EBOV 3d
D
EBOV
CXCL10
1 dpi
2 dpi
3 dpi

Figure S6. RNA FISH analysis of EBOV-infected iPSC-HLCs and Huh7 cells. (A) Ring chart displaying RNA FISH quantification data of *CXCL10*- or *IFNB1* -expressing cells shown in Figure 6. Shown is the percentage of uninfected and infected cells expressing either *CXCL10* (upper panel) or *IFNB1* (IFNβ, lower panel). (B) RNA FISH analysis of EBOV-infected iPSC-HLCs. RNA FISH probes target EBOV mRNA (green) and *IL6* mRNA (red). No red staining was detected. Scale bars are 10μm (C) Luminex analysis of BU1, BU2, and BU3 EBOV-infected and mock-infected iPSC-HLCs. Cells were infected with EBOV at an MOI 10 and cell supernatants were collected from infected and corresponding mock-infected controls 1, 2, and 3 dpi. CXCL10 protein expression was quantified from triplicate technical replicates using a Bioplex. (D) RNA FISH analysis of EBOV-infected Huh7 cells. Cells were infected at an MOI of 10 and fixed at the indicated time points. RNA FISH probes target EBOV mRNA (green) and *CXCL10* mRNA (magenta). No magenta staining was observed. Note that there is significant cell death at 2 and 3 dpi. Scale bars are 20μm.

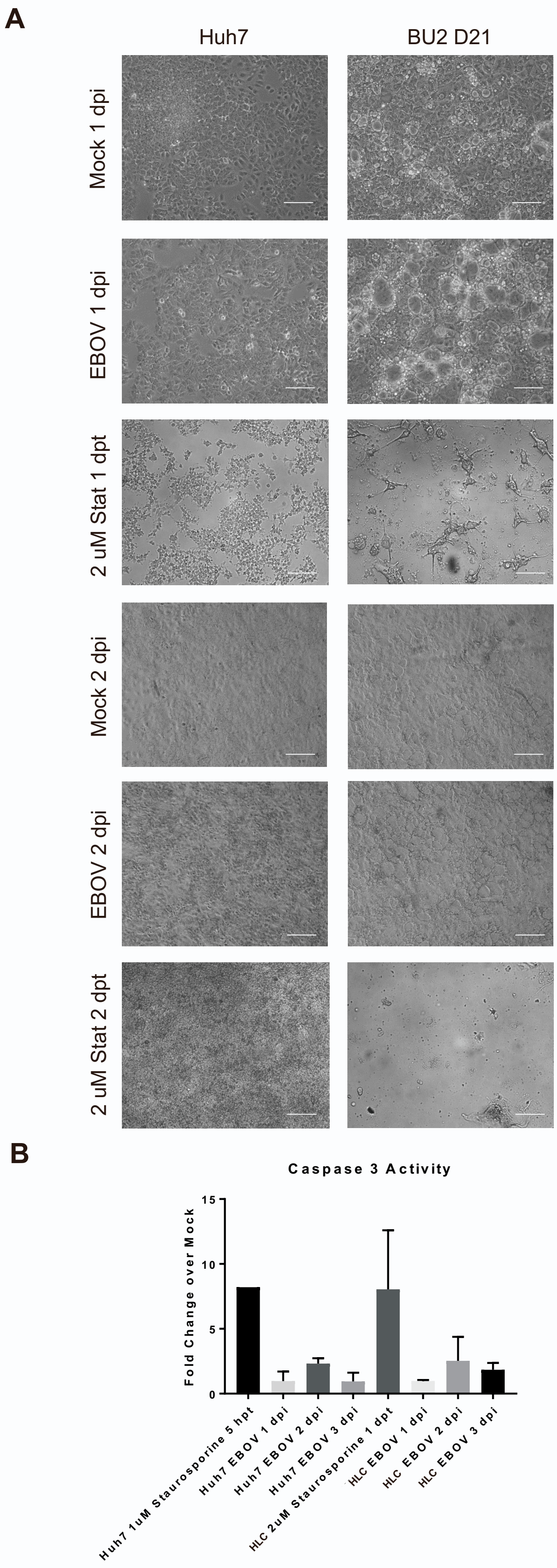
A
Huh7
BU2 D21
Mock 1 dpi
EBOV 1 dpi
2 uM Stat 1 dpt
Mock 2 dpi
EBOV 2 dpi
2 uM Stat 2 dpt
B
Caspase 3 Activity
Fold Change over Mock
15
10
5
0
Huh7 1uM Staurosporine 5 hpt
Huh7 EBOV 1 dpi
Huh7 EBOV 2 dpi
Huh7 EBOV 3 dpi
HLC 2uM Staurosporine 1 dpt
HLC EBOV 1 dpi
HLC EBOV 2 dpi
HLC EBOV 3 dpi

Figure S7. EBOV infection does not induce apoptosis in infected HLCs or Huh7 cells. (A) Brightfield images of Huh7 cells and BU2 HLCs either infected with EBOV MOI 10, mock infected, or treated with 2μM Staurosporine. Cells were imaged at the indicated time point. (B) Luminescence values of caspase 3 activity using the Promega Caspase-Glo 3/7 Assay kit. Triplicate samples of Huh7 cells and a single replicate each of bBU1, BU2, and BU3 HLCs were infected with EBOV MOI 10, mock infected, or treated with 2μM Staurosporine. Cell supernatants were harvested as the indicated time points and analyzed using a LUMIStar Omega Luminometer (BMG Labtech). Luminescent values were normalized to a blank control and reported as the fold change in luminescent activity over Mock-infected controls. Results from bBU1, BU2, and BU3 samples are averaged and represented as a single HLC sample.

Supplementary Tables

Gene Name	Adjusted p-value	logFC
COL3A1	9.58162E-09	2.079037109
ALB	1.10993E-06	0.791786818
GTF2A1	2.88433E-05	-0.823365329
ACTC1	8.32575E-05	0.166593898
HSPA1B	0.00012209	-1.932617071
HSD3B1	0.000145946	1.098272689
OR2I1P	0.000155119	0.483260067
COL1A2	0.000247591	1.28257751
HSPA1A	0.000373155	-2.049418845
CXCL2	0.000572529	0.671972125
AL161431.1	0.000793635	-0.541597932
EGR1	0.000793635	-0.668323271
ABCC3	0.001710955	-0.029215609
A2M	0.00178052	0.492236335
FMOD	0.001901718	0.699395715
ACTA1	0.002256423	0.144448347
TXNDC5	0.002626023	-1.819276835
MBNL3	0.002934011	0.863087837
AP000892.3	0.003258406	0.394206526
SAA1	0.003258406	0.0002776
TAGLN	0.003274745	0.424662869
AL355916.1	0.003274745	2.400345681
GDF15	0.003274745	-1.426469054
SPON2	0.003446481	0.509329633
H1FX	0.006171997	-1.404491248
ERRFI1	0.007591647	-0.595140628
CD24	0.00802999	0.930873507
MT-ATP6	0.00802999	1.065510209
POLR2A	0.00802999	-0.269318403
AP000648.3	0.008278758	-1.378343082
SRSF3	0.00844516	0.713503971
MX1	0.00844516	-1.76665914
MCAM	0.008722908	-0.504260289
TPM1	0.0091873	0.73398065

Table S1. Summary of host DEG at 1 dpi in EBOV-infected iPSC-HLCs. Transcripts were ranked) and sorted for transcripts with a False Discovery Rate adjusted p-value ≤ 0.01 when compared to the other time point and uninfected contrasts. The logFC of the transcript when compared to the uninfected iPSC-HLCs at 1 dpi is indicated in the logFC column (last column). logFC, log fold change compared to uninfected control.

Time Point	**Pathway**	**Leading Edge Number**	**Enrichment Score**	**FDR**
1 dpi	N/A			
2 dpi	Interferon alpha response	29	0.69408	0
	Interferon gamma response	51	0.59635	0
	TNFA signaling via NFkB	60	0.45735	0.0053618
	Blood vessel formation	24	-0.70587	0
	Epithelial mesenchymal transition	97	-0.44221	0.00066813
	Biosynthesis of bile acids	35	-0.48976	0.00083516
	Metabolism of xenobiotics	69	-0.47167	0.00083516
	Blood coagulation cascade	51	-0.48574	0.0011135
3 dpi	Interferon alpha response	31	0.70268	0
	Interferon gamma response	46	0.58008	0
	Oxidative phosphorylation and citric acid cycle	116	-0.58008	0
	MYC targets, variant 1	80	-0.40318	0.0015312
	Blood vessel formation	16	-0.60886	0.0015312
	Adipocyte development	77	-0.37443	0.0020416
	Reactive oxygen species pathway	30	-0.51705	0.0020416
	Epithelial mesenchymal transition	78	-0.38571	0.0024499
	Blood coagulation cascade	45	-0.40118	0.0034998
7 dpi	Metabolism of xenobiotics	47	-0.48082	0
	Blood coagulation cascade	39	-0.62257	0
	Biosynthesis of bile acids	30	-0.48532	0.0012961
	Unfolded protein response; ER stress	33	-0.45886	0.0077766
	Complement cascade	31	-0.41966	0.0089431

Table S2. Summary of Hallmark Pathway Analysis of EBOV-infected iPSC-HLCs. GSEA of Hallmark 50 Pathways for each time point of EBOV-infected iPSC-HLCs as compared to uninfected controls. Leading Edge Number represents the number of genes mapping to the hallmark pathway. Enrichment score is a measurement of the significance of the up or downregulation of the pathway based on the ranked genes that map to the particular pathway (closer to 1, more significantly upregulated; closer to -1, more significantly downregulated). Values greater than 0 are upregulated pathways, values less than 0 are downregulated pathways. FDR = false discovery rate. Parameters: minimum number of genes in a category = 15; FDR ≤ 0.01; number of permutations = 1000.

Antigen	**Company (catalog number)**	**Species**	**Dilution**
Albumin	Dako	Rabbit	1:100
Alexa Fluor α-mouse 594	Thermo Fisher (A32744)	Donkey	1:200

Alexa Fluor α-rabbit 488	Thermo Fisher (A48282)	Goat	1:200
Alexa Fluor α-goat 488	Thermo Fisher (A32814)	Donkey	1:200
CK18, human	Abcam (EPR1626)	Rabbit	1:100
EBOV NP	Gift from G. Olinger, USAMRIID	Mouse	1:200
EBOV VP35	Antagene, custom	Goat	1:1000
EBOV VP40	BEI	Mouse	1:200
FOXA1	Abcam (ab173287)	Rabbit	1:100
FOXA2	Abcam (ab108422)	Rabbit	1:100
HNF4α	Abcam (ab41898)	Mouse	1:50
NFκB p65 (A)	Santa Cruz (sc-8008)	Rabbit	1:200
Transferrin	ThermoFisher (MA5-29600)	Rabbit	1:50

Table S3. Antibodies used for immunofluorescence analysis. Not all antibodies in this table are commercially available at this time. In those cases, the catalog number has been omitted.

Medium Component	**Final Concentration or Volume**	**Source**
D5-D6		
Activin A	50 µg/mL	R&D Systems
BMP-4	10 ng/mL	Peprotech
FGF-2	10 ng/mL	Peprotech
VEGF	10 ng/mL	Peprotech
D7-D12		
Ascorbic Acid	50 µg/mL	Sigma Aldrich
BMP-4	50 ng/mL	Peprotech
FGF-2	10 ng/mL	Peprotech
VEGF	10 ng/mL	Peprotech
EGF	10 ng/mL	Peprotech
TGF-α	20 ng/mL	Peprotech
HGF	20 ng/mL	Peprotech
Dexamethasone	100 nM	Invitrogen
D13-D18		
FGF-2	10 ng/mL	Peprotech
VEGF	10 ng/mL	Peprotech
EGF	10 ng/mL	Peprotech

HGF	20 ng/mL	Peprotech
Dexamethasone	100 nM	Invitrogen
Oncostatin M	20 ng/mL	Peprotech
Vitamin K	6 ug/mL	Sigma Aldrich
DMSO	1%	Sigma Aldrich
γ-Secretase Inhibitor	1.5 μM	Calbiochem
D19-D30		
HGF	20 ng/mL	Peprotech
Dexamethasone	100 nM	Invitrogen
Oncostatin M	20 ng/mL	Peprotech
Vitamin K	6 μg/mL	Sigma Aldrich

Table S4. Differentiation protocol for hepatocyte-like cells from iPSCs. The concentration of each medium component and manufacturer are listed for each period of differentiation.

REFERENCES

Liao, Y., Wang, J., Jaehnig, E.J., Shi, Z., and Zhang, B. (2019). WebGestalt 2019: gene set analysis toolkit with revamped UIs and APIs. Nucleic Acids Res *47*, W199-W205. 10.1093/nar/gkz401.